Gravitational-Wave Parameter Inference with the Newman-Penrose Scalar

Juan Calderón Bustillo,[1,2,*] Isaac C. F. Wong,[2,†] Nicolas Sanchis-Gual,[3,4] Samson H. W. Leong,[2] Alejandro Torres-Forné,[3,5] Koustav Chandra,[6] José A. Font,[3,5] Carlos Herdeiro,[4] Eugen Radu,[4] and Tjonnie G. F. Li[2,7,8]

[1]*Instituto Galego de Física de Altas Enerxías, Universidade de Santiago de Compostela, 15782 Santiago de Compostela, Galicia, Spain*
[2]*Department of Physics, The Chinese University of Hong Kong, Shatin, New Territories, Hong Kong*
[3]*Departamento de Astronomía y Astrofísica, Universitat de València, Dr. Moliner 50, 46100 Burjassot (València), Spain*
[4]*Departamento de Matemática da Universidade de Aveiro and Centre for Research and Development in Mathematics and Applications (CIDMA), Campus de Santiago, 3810-183 Aveiro, Portugal*
[5]*Observatori Astronòmic, Universitat de València, C/ Catedrático José Beltrán 2, 46980 Paterna (València), Spain*
[6]*Department of Physics, Indian Institute of Technology Bombay, Powai, Mumbai, Maharashtra 400076, India*
[7]*Institute for Theoretical Physics, KU Leuven, Celestijnenlaan 200D, B-3001 Leuven, Belgium*
[8]*Department of Electrical Engineering (ESAT), KU Leuven, Kasteelpark Arenberg 10, B-3001 Leuven, Belgium*

(Received 28 June 2022; revised 17 November 2022; accepted 27 September 2023; published 12 December 2023)

Detection and parameter inference of gravitational-wave signals from compact mergers rely on the comparison of the incoming detector strain data $d(t)$ to waveform templates for the gravitational-wave strain $h(t)$ that ultimately rely on the resolution of Einstein's equations via numerical relativity simulations. These, however, commonly output a quantity known as the Newman-Penrose scalar $\psi_4(t)$ which, under the Bondi gauge, is related to the gravitational-wave strain by $\psi_4(t) = d^2h(t)/dt^2$. Therefore, obtaining strain templates involves an integration process that introduces artifacts that need to be treated in a rather manual way. By taking second-order finite differences on the detector data and inferring the corresponding background noise distribution, we develop a framework to perform gravitational-wave data analysis directly using $\psi_4(t)$ templates. We first demonstrate this formalism, and the impact of integration artifacts in strain templates, through the recovery of numerically simulated signals from head-on collisions of Proca stars injected in Advanced LIGO noise. Next, we reanalyze the event GW190521 under the hypothesis of a Proca-star merger, obtaining results equivalent to those previously published [Phys. Rev. Lett. **126**, 081101 (2021)], where we used the classical strain framework. We find, however, that integration errors would strongly impact our analysis if GW190521 was 4 times louder. Finally, we show that our framework fixes significant biases in the interpretation of the high-mass gravitational-wave trigger S200114f arising from the usage of strain templates. We remove the need to obtain strain waveforms from numerical relativity simulations, avoiding the associated systematic errors.

DOI: 10.1103/PhysRevX.13.041048 Subject Areas: Astrophysics, Gravitation

I. INTRODUCTION

The observation of the gravitational-wave (GW) event GW150914 in 2015 by the Advanced LIGO detectors [1] opened a new window to explore the Universe [2]. In barely half a decade, and after the addition of the Advanced Virgo [3] and KAGRA [4] detectors, the number of detections has grown to 90 events, all consistent with the merger of compact objects such as black holes (BHs) and neutron stars [5–8]. These events have provided us with invaluable knowledge about the BH population of our

*juan.calderon.bustillo@gmail.com
†cfwong@link.cuhk.edu.hk

Universe [9,10] and their environments, star formation, tests of strong gravity [11–19], and the observation of new strong-field phenomena [20–24] to name a few. The retrieval of this information relies on an accurate extraction of the parameters of the GW source. This is commonly carried out through the comparison of the incoming strain detector data $d(t)$ to precomputed waveform templates for the gravitational-wave strain $h(t;\theta)$ [25–29] that span a continuous range of possible source parameters θ such as the masses and spins of merging compact objects. In this process, it is crucial that waveform templates are faithful representations of the incoming GWs. For the case of the GWs emitted during the early inspiral, these templates can be obtained through analytical approximated techniques such as post-Newtonian approximations [30] or effective-one-body formalisms [31,32]. However, modeling the full space-time dynamics taking place during the merger and ringdown stages of compact binary mergers requires solving the full Einstein equations for the system, which can only be done through numerical simulations using numerical relativity (NR) [33–44]. Consequently, approximated models are commonly calibrated to these simulations during the merger and ringdown stages [45–51]. Alternatively, "surrogate" models can also be constructed by interpolating through a given set of NR simulations [52–54].

When available, NR provides the most accurate prediction for the GW emission of a given source. Therefore, if simulations are available in the parameter space of interest, a direct comparison of GW data to NR simulations is fundamental to—at least—check the robustness of the results provided by approximated models [55,56]. Furthermore, in some cases such as highly eccentric or precessing sources, continuous semianalytical models may not exist, leaving NR as the only option to analyze the data. Consequently, several studies have directly compared some of the existing signals to NR templates [55–58] and even used the latter as simulated signals to evaluate the efficacy of parameter estimation and detection algorithms [59–63].

Continuous models that include the entire inspiral-merger-ringdown process can only be built for regions of the parameter space densely covered by the available numerical simulations, namely sources with small orbital eccentricity and relatively equal masses. While these examples have sufficed to explain all GW signals detected to date, we are entering an era in which comparison with more exotic scenarios, for which only NR waveforms exist, is in order. Moreover, as of now, NR provides the only way to accurately model the dynamics of exotic compact objects and search for new physics beyond the neutron-star and Kerr black hole paradigm. For example, in Ref. [64] we recently compared GW190521 to numerical simulations of head-on mergers of exotic horizonless objects known as Proca stars, demonstrating that the latter scenario is slightly more consistent with the data than the standard one based on BBH mergers.

II. EXTRACTION OF GRAVITATIONAL-WAVE STRAIN FROM NUMERICAL SIMULATIONS VIA THE NEWMAN-PENROSE (NP) SCALAR ψ_4

While current GW detectors output a quantity known as GW strain $h(t)$, the most extended type of NR simulations, which are based on the $3+1$ formulation (or Cauchy evolution), return the so-called Newman-Penrose (NP) scalar $\psi_4(t)$ [65,66]. Under the Bondi gauge, the scalar $\psi_4(t)$ is related to the strain by $\psi_4(t) = d^2h(t)/dt^2$ [67]. Obtaining $h(t)$ therefore requires a double time integration, which is a nontrivial process involving fundamental difficulties. A well-known effect is the appearance of nonlinear drifts in the resulting strain waveform arising from the *time-domain integration* of finite length, discretely sampled and noisy data streams. These are independent of the parameters of the simulation, such as gauge or numerical method used [68].

Frequency-domain integration methods can avoid the effects arising from time-domain integration but at the cost of modifying the original data. One of the best-known effects is the impact of spurious low-frequency modes in the strain waveform. It is known that the effect of these modes, resulting from either spectral leakage or aliasing effects, can be significantly suppressed through the usage of high-pass signal filters [68,69] that can reduce the energy within frequencies lower than a chosen cutoff ω_0. This technique is commonly known as "fixed-frequency integration" (FFI). A common and well-motivated choice for ω_0 is that corresponding to the lowest instantaneous frequency of the GW emission. This is, for instance, the strategy used by the existing parameter-estimation code RIFT [57] to directly compare GW data to NR templates. In practice, however, the choice of ω_0 requires a certain amount of tuning. On the one hand, a small value will amplify nonphysical low-frequency components during the integration process. On the other hand, a large value may suppress the physical frequencies of the waveform. In some cases, such a choice can be clearly guided by the known features of the "true" signal. For instance, in the case of quasicircular binaries, the inspiral GW "chirp" frequency is a monotonically increasing function of time, which provides a natural way to associate a given choice of ω_0 with a given starting time for the strain waveform.

This choice, however, is not obvious or even well defined for cases where the GW frequency is not a monotonic function of time. On the one hand, this makes FFI itself a potential source of error that, as we will show, can qualitatively impact the interpretation of the source. On the other hand, in the best-case scenario, a "correct" obtention of the strain data requires an artisan and time-consuming trial-and-error process adapted to each particular type of source. This is the case of some of the most interesting sources that the astrophysical community is trying to detect for the first time in the next observing run of LIGO and Virgo. Such cases include eccentric mergers [58], highly

precessing mergers, dynamical captures [70], or even cases in which an inspiral stage does not exist at all. This is also the situation for the (academic) case of head-on collisions [71] that we will address in this work or for core-collapse supernovae waveforms, for which the bounce GW signal consists essentially of a burst [72–74]. Finally, the act of integrating involves a choice of integration constants that can cause fundamental changes in the properties of the waveform. For instance, it is typically imposed that the average of the GW strain should be zero, which automatically removes or changes the effect of GW memory [75].

Integration-free extraction methods. While in this work we focus on numerical waveforms obtained through the NP formalism, whose use is much generalized in the numerical relativity community, we note that there exist alternative methods that can directly extract the GW strain. First, within the Cauchy evolution framework, the GW strain can also be directly extracted at finite radii through the so-called Regge-Wheeler-Zerilli (RWZ) method [76–78]. Just as in the NP case, waveforms can then be extrapolated to null infinity through, e.g., polynomial expansions [40,79]. RWZ extraction has been long employed by the SXS Collaboration [40], producing extensive catalogs of BBH waveforms that include the largest number of inspiral cycles in the literature. These waveforms have been consistently used to inform continuous waveform models (see, e.g., Ref. [53]), often in combination with waveforms obtained through the NP formalism (see, e.g., Refs. [49,50]), and to directly analyze several GW events [55,56]. Second, within the so-called Cauchy characteristic extraction framework [80], waveforms can be directly extracted at future null infinity. While early simulations were limited to output the Bondi news function [81] [given by $\mathcal{N}(t) = dh(t)/dt$], later developments made possible the direct extraction of the GW strain [82–84], including some simulations in the SXS catalog [84].

While the above approaches present advantages with respect to the NP formalism, there are reasons that motivate the generalized use of the latter. First, the master wave equations of the RWZ approach are obtained under the assumption that the background metric can be described by a Schwarzschild space-time where perturbations are applied. Also, it has been found that the relative accuracy of RWZ and NP methods depends on the case of application; see, e.g., Refs. [85,86]. Second, while the Cauchy characteristic extraction can deliver extremely accurate waveforms, it involves specific complications that have so far prevented its widespread use, on top of its intensive computational cost. For instance, recent studies have discussed the weak hyperbolicity of the characteristic evolution equations [87–89]. Also, initial spurious emission known as junk radiation has been found to last significantly longer in these simulations [84]. In addition, characteristic evolution (based on null foliations) is known to be limited to describe BBH systems, as null surfaces may

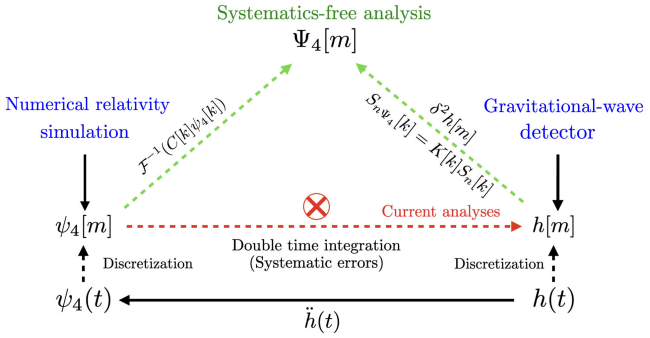

FIG. 1. Schematic comparison of our proposed data analysis framework and the currently used one. To date, the ψ_4 magnitude outputted by numerical relativity simulations is converted to the strain h outputted by gravitational-wave detectors via a double integration that is subject to systematic errors (red path). Instead, we transform both the simulation ψ_4 and the detector h (and power spectral density S_n) into a third quantity that we label by Ψ_4, avoiding the integration process and the corresponding systematic errors (green paths).

focus and form caustics [81]. This triggered the design of so-called Cauchy characteristic matching methods [89,90]. Finally, we note that NP presents several advantages of its own, as enumerated in Ref. [66]. (a) It provides a first-order, gauge-invariant description of the radiation field (see Koop and Finn [91] for a fully gauge-invariant derivation of the detector response), (b) it does not rely on any frequency or multipole decomposition, and (c) the Weyl scalars (ψ_4 among them) are defined in the full nonlinear theory. A one-parameter perturbative expansion of this theory was proved to provide a reliable account of the problem [92]. And (d), finally, the NP formulation provides a simpler framework to organize higher-order perturbation schemes. For an overview of different waveform extraction methods, we refer the reader to Ref. [93].

In this work we remove from GW data analysis the fundamental problems related to waveform integration by avoiding such a step. We present a framework, schematically summarized in Fig. 1, to perform GW data analysis directly using $\psi_4(t)$. This provides a uniquely defined way to obtain GW waveforms for data analysis—free of human choices—which are by definition free of the systematic errors related to waveform integration. We showcase our framework in the context of parameter inference and model selection performed on both synthetic signals injected in LIGO-Virgo noise and on real GW signals.

III. OUR CASE OF STUDY: MERGERS OF PROCA STARS

A. Proca stars and dark matter

Proca stars belong to a family of theoretical exotic compact objects (ECOs) known as bosonic stars [94–97]. These are part of the wider family of objects known as "BH mimickers" which, lacking the characteristic event

horizon of BHs, can reproduce many of their properties, see, e.g., Refs. [98–100], avoiding issues related to the black hole singularity, as well as poorly understood issues related to quantum fields near event horizons [101]. ECOs have been proposed, e.g., as dark matter candidates [102], in particular in models invoking the existence of hypothetical ultralight (i.e., sub-eV) bosonic particles, often referred to as fuzzy dark matter [103]. One common candidate is the pseudo-scalar QCD axion [104], but other ultralight bosons arise, e.g., in the string axiverse [105]. In particular, vector bosons are also motivated in extensions of the standard model of elementary particle [106] and can clump together forming macroscopic entities dubbed vector boson stars or Proca stars.

Bosonic stars are among the simplest and dynamically more robust ECOs proposed so far and their dynamics have been extensively studied; see, e.g., Refs. [71,107–109]. Scalar boson stars and their vector analogs, Proca stars [95,110], are self-gravitating stationary solutions of the Einstein (complex, massive) Klein-Gordon [94] and of the Einstein (complex) Proca [95] systems, respectively. These consist of complex bosonic fields oscillating at a well-defined frequency ω, which determines the mass and compactness of the star. Bosonic stars can dynamically form without any fine-tuned condition through the gravitational cooling mechanism [111,112].

While spinning solutions have been obtained for both scalar and vector bosons, the former are unstable against nonaxisymmetric perturbations, in the simplest models wherein the bosonic field is free [113,114]. Hence, we will focus on the vector case in this work. For non-self-interacting bosonic fields, the maximum possible mass of the corresponding stars is determined by the boson particle mass $\mu_{\rm B}$. In particular, ultralight bosons within $10^{-13} \leq \mu_{\rm B} \leq 10^{-10}$ eV can form stars with maximal masses ranging between $\sim$1000 and 1 solar masses, respectively. In Ref. [64], we showed that GW190521 was consistent with the head-on collision of two Proca stars with $\mu_{\rm B} = 8.7 \times 10^{-13}$ eV.

B. Numerical simulations of Proca-star mergers

We will demonstrate our ψ_4 data analysis making use of NR simulations of head-on collisions of spinning Proca stars. In addition to the quadrupole $(\ell, m) = (2, \pm 2)$ modes dominant for circular mergers, our simulations also yield the (2, 0) mode, codominant for the case of head-on collisions, and the much weaker $(3, \pm 3)$ and $(3, \pm 2)$ modes. Our set of waveforms is obtained from simulations of the collisions of two spinning Proca stars with aligned spin axes [64,115,116]. Although starting from rest, the trajectories of the two stars are eccentric rather than strictly head-on due to frame dragging. In our study's region of parameter space, all Proca-star progenitors are sufficiently massive and compact to trigger the gravitational collapse of the remnant. Therefore, the outcome of the collision always leads to BH formation after the merger. The simulations are performed with the EINSTEIN TOOLKIT infrastructure [117,118], together with the CARPET package [119,120] for mesh refinement. The Proca evolution equations are solved via a modified Proca thorn [71,113,121,122] to include a complex field. We consider both equal-mass and unequal-mass cases, as reported in our numerical Proca catalog [116]. The initial data consist of the superposition of two equilibrium solutions separated by $D = 40/\mu$ [64,71,109,123], in geometrized units, guaranteeing an admissible initial constraint violation. The equilibrium stars are numerically constructed using the solver fidisol/cadsol for nonlinear partial differential equations of elliptic type, via a Newton-Raphson method (see Refs. [95–97] for more details).

IV. DATA ANALYSIS WITH ψ_4

Consider an observation model,

$$\begin{aligned} d(t) &= F_+ h_+(t) + F_\times h_\times(t) + n(t) \\ &= s(t) + n(t), \end{aligned} \tag{1}$$

where $s(t) = F_+ h_+(t) + F_\times h_\times(t)$ is the GW strain, F_+ and $F_\times$ are the beam pattern functions of the $+$ and $\times$ polarization states, i.e., $h_+(t)$ and $h_\times(t)$, respectively, and $n(t)$ is the detector noise. Here we only consider a transient signal; therefore, the beam pattern functions are approximated to be constant over the duration of the signal for a given sky localization and polarization angle. We can rewrite Eq. (1) as follows:

$$\begin{aligned} d(t) &= \mathrm{Re}\{(F_+ + iF_\times)[h_+(t) - ih_\times(t)]\} + n(t) \\ &= \mathrm{Re}[(F_+ + iF_\times)h(t)] + n(t), \end{aligned} \tag{2}$$

where $h(t) = h_+(t) - ih_\times(t)$. Taking second-time derivative on both sides yields

$$\begin{aligned} \frac{d^2 d(t)}{dt^2} &= \mathrm{Re}[(F_+ + iF_\times)\psi_4(t)] + \frac{d^2 n(t)}{dt^2} \\ &= s_{\psi_4}(t) + \frac{d^2 n(t)}{d^2 t}, \end{aligned} \tag{3}$$

where $\psi_4(t) = d^2 h(t)/dt^2$ and $s_{\psi_4}(t) = d^2 s(t)/dt^2$. Now we have obtained the observation model with $\psi_4(t)$ directly involved. Since in practice we analyze the digital strain data which are discrete, we have to replace the second-order differential operator d^2/dt^2 by the second-order difference operator δ^2 defined by

$$(\delta^2 x)[m] \coloneqq \frac{x[m+1] - 2x[m] + x[m-1]}{(\Delta t)^2}, \tag{4}$$

where $x[m]$ is a discrete-time series (labeled by index m) with a sampling interval Δt. We then have

$$(\delta^2 d)[m] = \mathrm{Re}\{(F_+ + iF_\times)(\delta^2 h)[m]\} + (\delta^2 n)[m]. \tag{5}$$

To express the above observation model with a closer notation connection to $\psi_4(t)$, i.e., the second derivative of $h(t)$, we put a subscript Ψ_4 to represent a second-order differenced time series, i.e., $x_{\Psi_4}[m] \coloneqq (\delta^2 x)[m]$. And we also reserve $\Psi_4[m]$ as a special notation for $(\delta^2 h)[m]$, in analogy with $\psi_4(t)$. With the new set of notations, we rewrite Eq. (5) as

$$\begin{aligned} d_{\Psi_4}[m] &= \mathrm{Re}\{(F_+ + iF_\times)\Psi_4[m]\} + n_{\Psi_4}[m] \\ &= s_{\Psi_4}[m] + n_{\Psi_4}[m], \end{aligned} \tag{6}$$

where $s_{\Psi_4}[m] = \mathrm{Re}\{(F_+ + iF_\times)\Psi_4[m]\}$ is the second difference of the GW strain signal. In practice, parameter estimation is often performed on the data in the Fourier domain due to the more efficient evaluation of the likelihood function as compared to that in the time domain (see, e.g., Ref. [14]). Applying Fourier transform on Eq. (6) yields

$$\tilde{d}_{\Psi_4}[k] = \frac{(F_+ + iF_\times)\tilde{\Psi}_4[k] + (F_+ - iF_\times)\tilde{\Psi}_4^*[-k]}{2} + \tilde{n}_{\Psi_4}[k]. \tag{7}$$

We note, however, that since the $\psi_4(t)$ extracted from NR simulations is sampled from the second derivative of $h(t)$, $\ddot{h}[m]$, *but not* the second-order finite difference of the discrete strain $(\delta^2 h)[m]$, we cannot directly use ψ_4 as templates for our analysis. Instead, as represented on the left-hand side of Fig. 1, we need to transform these following the relation

$$\tilde{\Psi}_4[k] = \frac{1 - \cos(2\pi k \Delta f \Delta t)}{2\pi^2 (k \Delta f \Delta t)^2} \tilde{\psi}_4(k\Delta f), \tag{8}$$

for which we provide the proof in Appendix A. In the above equation, $\Delta f = 1/(M\Delta t)$ and M is the length of the discrete $\Psi_4[m]$. We finally obtain the observation model in the Fourier domain with $\tilde{\psi}_4$ directly involved as follows,

$$\tilde{d}_{\Psi_4}[k] = \tilde{s}_{\Psi_4}[k;\theta] + \tilde{n}_{\Psi_4}[k], \tag{9}$$

where

$$\begin{aligned} \tilde{s}_{\Psi_4}[k;\theta = \{\alpha, \delta, \psi, t_{\mathrm{event}}, \theta'\}] &= \frac{1 - \cos(2\pi k \Delta f \Delta t)}{4\pi^2 (k \Delta f \Delta t)^2} [(F_+ + iF_\times)\tilde{\psi}_4(k\Delta f; \theta') \\ &\quad + (F_+ - iF_\times)\tilde{\psi}_4^*(-k\Delta f; \theta')], \end{aligned} \tag{10}$$

where F_+ and $F_\times$ are functions of the sky location of the source, i.e., the right ascension α, the declination δ, the polarization angle ψ, and the event time t_{event}, and θ' are other source parameters.

Another crucial ingredient for parameter estimation is the distribution of the second-differenced noise $\tilde{n}_{\Psi_4}[k]$ in order to obtain the likelihood function. It can be shown (see Appendix B) that if $n(t)$ follows the stationary Gaussian distribution with power spectral density $S_n(f)$, then $n_{\Psi_4}[m]$ also follows the stationary Gaussian distribution with power spectral density $S_{n_{\Psi_4}}[k]$ as

$$S_{n_{\Psi_4}}[k] = \frac{1}{(\Delta t)^4} \left[6 - 8\cos\left(\frac{2\pi k}{M}\right) + 2\cos\left(\frac{4\pi k}{M}\right)\right] S_n[k], \tag{11}$$

where $S[k]$ is understood to be $S(k\Delta f)$.

The likelihood function for source parameters θ given the second-differenced strain data d_{Ψ_4} in the Fourier domain is, therefore,

$$\mathcal{L}(d_{\Psi_4}|\theta) \propto \exp\left[-\frac{1}{2}[d_{\Psi_4} - s_{\Psi_4}(\theta)|d_{\Psi_4} - s_{\Psi_4}(\theta)]\right], \tag{12}$$

where $s_{\Psi_4}(\theta)$ is the second-differenced template with parameters θ, and $(a|b)$ denotes the noise-weighed inner product defined as [124]

$$(a|b) = 4\mathrm{Re}\int_{f_{\min}}^{f_{\max}} \frac{\tilde{a}^*(f)\tilde{b}(f)}{S_{n_{\Psi_4}}(f)} df, \tag{13}$$

with $S_{n_{\Psi_4}}(f)$ the power spectral density of the second-differenced detector noise given in Eq. (11).

A. Summarized recipe for a ψ_4 analysis

We summarize here our method to perform GW data analysis with ψ_4. Consider the canonical situation where we have detector strain data $d(t)$, the corresponding power spectral density (PSD) $S_n(f)$, and strain templates $s(t;\theta)$ for source parameters θ. Then, an analysis based on the Newman-Penrose scalar can be implemented by just replacing the following:

$$\begin{aligned} &\text{Data:} \quad d(t) \to d_{\Psi_4}(t) \equiv (\delta^2 d)(t) \quad [\text{Eq.}(4)], \\ &\text{PSD:} \quad S_n(f) \to S_{n_{\Psi_4}}(f) \quad [\text{Eq.}(11)], \\ &\text{Templates:} \quad \tilde{s}(f;\theta) \to \tilde{s}_{\Psi_4}(f;\theta) \quad [\text{Eq.}(8)]. \end{aligned} \tag{14}$$

Above, we assume that Ψ_4 templates are obtained from the ψ_4 outputted by NR simulations through Eq. (8), i.e., following the right path of Fig. 1, and are therefore free of integration systematics present in the strain templates. Consequently, both sides of Eq. (14) generally lead to

different results, which is the point of our work. Nevertheless, one can also check that obtaining Ψ_4 as $\delta^2 h$ following the left-hand side of Fig. 1 (taking second-order finite differences on the strain templates) makes both sides of Eq. (14) return identical results.

V. RESULTS: DATA WHITENING

GW data analysis ultimately relies on whitened data; that is, the detector data divided by the amplitude spectral density of the background noise $\tilde{d}(f)/\sqrt{S_n(f)}$. This is then matched filtered [25] with the whitened waveform templates $\tilde{h}(f)/\sqrt{S_n(f)}$. Here we show that the transformations we perform on both the strain data and PSD to obtain their $\Psi_4(t)$ versions lead to identical whitened data and templates. Therefore, these lead to a completely equivalent analysis where the only difference is that $\Psi_4(t)$ templates are free of systematic errors introduced during the obtention of the $h(t)$ templates through integration.

A. Analytic case: Sine-Gaussian waveform

We start by considering the case of an analytical function $h(t)$ for which we can analytically compute $\psi_4(t) = d^2h(t)/dt^2 \equiv \ddot{h}(t)$. This way, we have a "controlled" experiment where the "strain" $h(t)$ and the corresponding "Newman-Penrose scalar" $\psi_4(t)$ at hand are free of potential differences introduced by systematic errors arising from the double integration of the former. In particular, we consider the case of a sine-Gaussian strain time series:

$$h(t) = A_0 e^{-(t-t_0)^2/\tau} \cos(\omega t + \phi_0). \tag{15}$$

For this strain, we compute the corresponding $\psi_4(t)$ and obtain a corresponding finite sampling time series $\psi_4[m]$. Next, we obtain a finite sampling time series of the strain $h[m]$ and compute the corresponding second-order difference $\Psi_4[m] \equiv (\delta^2 h)[m]$. Finally, we also obtain $\delta^2 h[m]$ by "correcting" the discretized second derivative $\ddot{h}[m]$, via the transformation in Eq. (8). The left-hand panel of Fig. 2 shows these three time series. The inset therein shows that while the two finite-differenced time series are identical, $\ddot{h}(t)$ differs from them.

Next, we compare the result of whitening the strain time series $h[m]$ by a given strain PSD S_n and that of whitening $\delta^2 h[m]$ by the corresponding transformed PSD $S_{n_{\Psi_4}}$. The inset of the right-hand panel of Fig. 2 shows the difference between the whitened Fourier transforms of $h[m]$ and $\delta^2 h[m]$. As before, we obtain the latter both by taking second-order finite differences on $h[m]$ and by correcting $\ddot{h}[m]$ via Eq. (8), which we denote $\ddot{h}_{\rm corr}$. These differences are below 1 part in 10^{12}. The main panel shows the differences between the whitened $h[m]$ and $\ddot{h}[m]$, "wrongly" whitened by $S_{n_{\Psi_4}}$, which are 9 orders of magnitude larger.

The above shows that given a continuous strain $h(t)$ and its corresponding $\psi_4(t) \equiv \ddot{h}(t)$, the processes of (a) taking second-order finite differences on the finite-sampling time series of $h[m]$ and (b) correcting $\ddot{h}[m]$ via Eq. (8) lead to identical time series that we call $\Psi_4(t)$. Second, it shows that given the PSD of a stochastic Gaussian and stationary strain time series $h[m]$ and the corresponding $(\delta^2)h[m] = \Psi_4[m]$, our estimation of the PSD $S_{n_{\Psi_4}}$ correctly whitens the latter. In the following, in order to adapt to common literature, we drop the discrete notation, e.g., replacing $h[m]$ by $h(t)$.

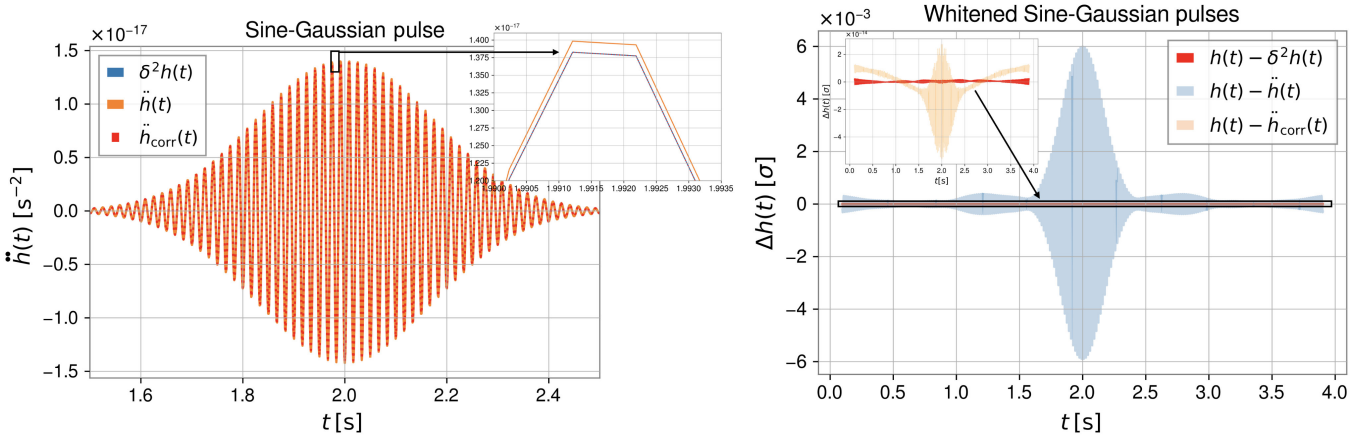

FIG. 2. Demonstration of our transformation and whitening scheme on sine-Gaussian pulses. The left-hand panel shows the analytical second derivative $\ddot{h}(t)$ of a sine-Gaussian strain time series $h(t)$ and its second-order finite-difference time series $\delta^2 h(t)$. We obtain the latter both directly and from correcting $\ddot{h}(t)$ via Eq. (8). The inset shows that $\ddot{h}$ differs from the other two curves. The inset of the right-hand panel shows the difference between the latter two time series, whitened with a PSD $S_{n_{\Psi_4}}$, and the original strain $h(t)$ whitened by the corresponding S_n. These are of the order of 1 part in 10^{12}. The main right-hand panel shows the (much larger) difference between the whitened strain and second derivative $\ddot{h}(t)$ whitened with $S_{n_{\Psi_4}}$.

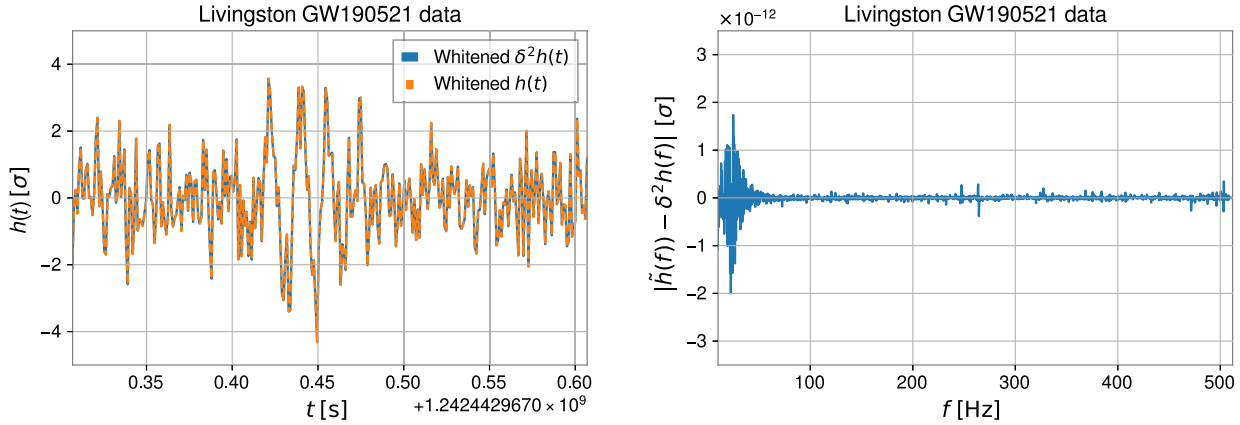

FIG. 3. Whitening of strain and Ψ_4 detector data. Left: whitened strain and Ψ_4 gravitational-wave time series from the Livingston detector around the time of GW190521. Right: difference between the absolute values of the corresponding Fourier-domain data. These are at the level of 1 part in 10^{12}, so that both whitened detector data are equivalent for all practical purposes.

B. Whitening of detector data

The left-hand panel of Fig. 3 shows the whitened strain $d(t)$ and $d_{\Psi_4}(t)$ time series of the Livingston detector at the time of the event GW190521. Their differences, shown in the right-hand panel, are well below 1 part in 10^{12}. Again, this shows that our formalism correctly whitens the data and that, therefore, both types of analyses are totally equivalent provided that no artifacts are picked during the construction of the strain templates from the ψ_4 templates.

1. Whitening waveform templates: Impact of the choice of ω_0 during fixed-frequency integration

The left-hand panels of Figs. 4 and 5 show raw strain templates obtained from two simulations of a Proca-star merger $h(t)$. These, respectively, correspond to a waveform consistent with GW190521 and to a larger mass ratio and rather edge-on configuration with multimodal structure [21,125,126] that, in a separate paper [127], we find consistent with the GW trigger 200114_020818 (S200114f in the following) [128] (see the specific parameters in Appendix C). In both cases, the strain $h(t)$ has been obtained from $\psi_4(t)$ through an FFI using a given ω_0 cutoff. Overlaid, we show the corresponding $\Psi_4(t)$ obtained both as $(\delta^2 h)(t)$ and by correcting $\psi_4(t)$ outputted by NR, which in the following we simply call $\Psi_4(t)$. We scale $h(t)$ by a suitable amplitude factor so that both waveforms can be plotted together. The right-hand panel shows the corresponding whitened waveforms.

First, we note that while (as expected) the raw $h(t)$ widely differs from the two $\Psi_4(t)$ waveforms, the whitened

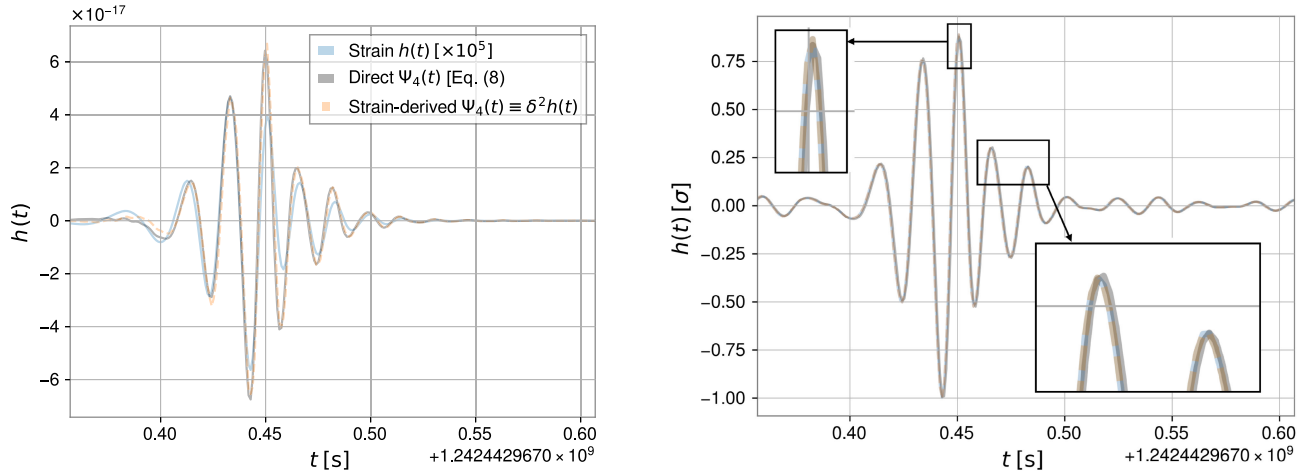

FIG. 4. Whitening of strain and Ψ_4 templates. Left: we show the raw time-domain data for the case of (a) Ψ_4 directly coming from a numerical relativity simulation [through Eq. (8)] of a head-on Proca-star merger consistent with GW190521 (black), (b) the strain obtained from ψ_4 through double integration (blue), and (c) the Ψ_4 obtained from the latter through second-order finite differencing, denoted by $\delta^2 h(t)$. The strain in the left-hand panel has been conveniently scaled to note the obvious morphological differences with respect to Ψ_4. Right: corresponding whitened time series. The enlarged boxes show how the $h(t)$ and $\delta^2 h(t)$ are exactly identical while very small differences can be observed with respect to the original Ψ_4.

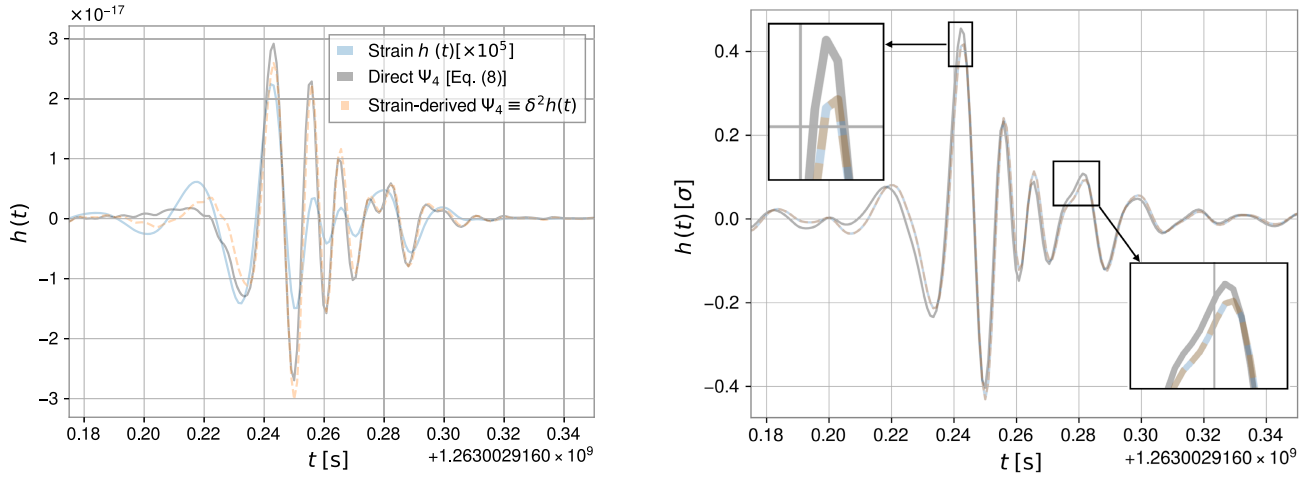

FIG. 5. Whitening of strain and Ψ_4 templates. Impact of aggressive choice of ω_0. Same as in Fig. 4 but for a waveform template consistent with S200114f [127,128]. In this case, the differences between the Ψ_4 directly extracted from the numerical simulation and the other two waveforms are significantly more noticeable.

$h(t)$ and $(\delta^2 h)(t)$ waveforms are identical but differ from the "direct" Ψ_4. This is due to the impact of the choice of ω_0 used to obtain $h(t)$ from $\psi_4(t)$. As we will show later, for the case shown in Fig. 4, these differences are not large enough to have a significant impact on parameter inference or model selection. However, for the case shown in Fig. 5, the choice of ω_0 removes enough "true" signal power to cause clear morphological alterations that impact both parameter estimation and model selection.

VI. PARAMETER INFERENCE AND MODEL SELECTION ON SIMULATED SIGNALS

A. Summary of Bayesian parameter inference and model selection

We test our framework by performing full Bayesian parameter estimation and model selection on simulated signals injected in zero noise using the Bayesian inference library PARALLEL BILBY. We consider a reference signal or "injection" $h_M(\theta_{\rm True})$ with source parameters $\theta_{\rm True}$ computed by a waveform model M. In our case, the model M corresponds to either $\Psi_4(t)$, $h(t)$, or $(\delta^2 h)(t)$. Next, we recover the posterior distributions of the parameters $p_{M^*}[\theta|h(\theta_{\rm True})]$ using a different model M^* as the signal template. This is given by

$$p_{M^*}[\theta|h_M(\theta_{\rm true})] = \frac{\mathcal{L}_{M^*}[h_M(\theta_{\rm True})|\theta]\pi(\theta)}{\mathcal{Z}_{MM^*}}. \quad (16)$$

Here, $\pi(\theta)$ denotes the prior probability of the parameters θ while $\mathcal{L}_{M^*}[h_M(\theta_{\rm True}]|\theta)$ represents the likelihood of the data $h_M(\theta_{\rm True})$ under the waveform model M^* with the given parameters θ. We use the canonical likelihood for GW transients in Eq. (12). Finally, the term $\mathcal{Z}_{MM^*}$ denotes the Bayesian evidence for the data h_M assuming the template model M^*. This is equal to the integral of the numerator over the explored parameter space Θ, given by

$$\mathcal{Z}_{MM^*} = \int_\Theta \pi(\theta)\mathcal{L}_{M^*}[h_M(\theta_{\rm True})|\theta]d\theta. \quad (17)$$

Given two template models M_1 and M_2 being compared to some data d, or some simulated signal $h_M(\theta)$, the relative probability for those models, or relative Bayes factor $\mathcal{B}^{M_1}_{M_2}$, is given by

$$\mathcal{B}^{M_1}_{M_2} = \frac{\mathcal{Z}_{M_1}}{\mathcal{Z}_{M_2}}. \quad (18)$$

Expressing these in terms of natural logarithms, it is commonly considered that the model M_1 is strongly preferred with respect to M_2 when $\log(\mathcal{B}^{M_1}_{M_2}) = \log(\mathcal{Z}_{M_1}) - \log(\mathcal{Z}_{M_1}) \geq 5$. Finally, since the Bayesian evidence $\mathcal{Z}$ represents the Bayes factor for the "model vs noise" hypotheses, we will commonly refer to it as simply the "Bayes factor," denoting it as $\mathcal{B}$.

As it will become relevant later, it is important to note that the evidence $\mathcal{Z}_{MM^*}$ is bounded above by the maximum value of the likelihood $\mathcal{L}_{M^*}[h_M(\theta_{\rm True})|\theta_{\rm best}]$, achieved for the best fitting parameters $\theta_{\rm best}$, this is, by the best fit that the model M^* can provide for $h_M(\theta)$. At the same time, in the absence of noise, such maximum likelihood is capped by the "optimal maximum likelihood" $\mathcal{L}_M[h_M(\theta_{\rm True})|\theta_{\rm True}]$.

To anticipate the expected consequences of respectively analyzing and modeling a true GW using a template affected by integration errors, let us consider two scenarios. First, consider that we model the true GW, i.e., our injection, as $h_M(\theta_{\rm True}) = \Psi_4(\theta_{\rm True})$ and try to recover it using templates $(\delta^2 h)(\theta_{\rm True})$ which carry integration

artifacts. Since such artifacts will change the frequency content of the templates, these will not perfectly match the injection, leading to a drop in the maximum likelihood and, therefore, of the corresponding Bayesian evidence in favor of the model. Second, any choice of the integration frequency cutoff ω_0 will remove some true power from the waveform. This will consequently lead to an underestimation of the signal loudness for a given source distance, yielding a bias toward lower distances. Third, for this last reason, if we model the true signal using either $h(\theta_{\rm True})$ or $(\delta^2 h)(\theta_{\rm True})$, this will cause an underestimation of the signal loudness, the optimal maximum likelihood and, therefore, an intrinsic decrease of the maximum Bayesian evidence achievable in the analysis.

B. Specific setup

We perform parameter estimation on injections generated in terms of $\Psi_4(t)$, $h(t)$, and $(\delta^2 h)(t)$. For the latter two, we consider two cases. In the first case, we obtain the strain through FFI using a frequency cutoff $M\omega_0 \simeq 0.27$, in geometric units [129]. In the second case, we simply apply a regularization at the pole given by $\omega_0 = 0$, which we replace by the value for the lowest frequency multiplied by 10^{-4}. We respectively label the resulting waveforms by F and NF subindexes, i.e., $h_{\rm F}$ $(\delta^2 h_{\rm F})$ and $h_{\rm NF}$ $(\delta^2 h_{\rm NF})$.

We recover these injections using different types of templates, as shown in Table I. We make two choices for the parameters θ, corresponding to the two cases shown in Figs. 4 and 5. These correspond to parameters consistent with GW190521 and the trigger S200114f under our Ψ_4 formalism. The most relevant difference between the corresponding simulations is the aggressiveness of the ω_0 used to obtain $h(t)$.

As mentioned in the previous section, in the case of the simulation consistent with GW190521, we find that this does not subtract significant power from the portion of the signal falling into the Advanced LIGO sensitive band while in the second case (the S200114f-like simulation) it does. The expectation is that for the first case, results obtained through Ψ_4 and all $h_{\rm F}$-based analyses will be very similar; while in the second, those based on filtered waveforms will differ significantly. In particular, two types of differences are expected. First, if the frequency content of the waveforms is altered by the integration errors, this will limit the ability of the resulting strain waveforms [or rather, $(\delta^2 h)(t)$] to fit the original Ψ_4. This will translate into both a reduction of the Bayes factor that may bias model selection and into potential parameter biases. Second, since any choice of ω_0 will remove a certain amount of signal power, this will result in an underrating of the strain-signal loudness. On the one hand, for identical parameters, this will lead to an underestimation of the signal SNR. On the other hand, this will cause a bias in the distance estimate.

The significance of the above effects in model selection and parameter inference depends on the signal loudness, as louder signals require more accurate templates in order to avoid analysis biases. We evaluate the impact of these biases under various observing scenarios; we consider three types of signal loudness, characterized by the optimal signal-to-noise ratio of the injection modeled by Ψ_4. In the first case, we use the parameters best fitting GW190521 and S200114f, making the Ψ_4 injection have an SNR of $\simeq$15 across the whole detector network, typical of current GW detections. Next, reducing the distance by a factor of 2, we study the case of signals with SNR $\simeq$ 30, similar to the maximum SNR observed to date. Finally, we consider the case where the injection has an SNR of $\simeq$60. For simplicity, in what follows, we will use "=" signs to refer to these cases.

Finally, as shown in the previous section, if our Ψ_4 formalism is equivalent to the classical one based on strain, results obtained through the injection and recovery of

TABLE I. Summary of injection recovery with different waveform models. We report the log Bayes factor (for model M^* vs noise hypotheses) obtained from our different waveform models, together with the corresponding maximum log-likelihood values. We show results for two types of injections of Proca-star merger signals, respectively consistent with the GW190521 signal and with the S200114f trigger, both with SNRs around 15. To show the increasing impact of ψ_4 integration errors as the SNR raises, we further scale our injections by factors of 2 and 4, corresponding to SNRs of approximately 30 and 60. Log Bayes factors have typical uncertainties of $\simeq$0.1. with maximum values of 0.5.

Waveform model		GW190521-like injection						S200114f-like injection					
		SNR = 15		SNR = 30		SNR = 60		SNR = 15		SNR = 30		SNR = 60	
Injection M	Template M^*	$\log \mathcal{B}$	$\log \mathcal{L}_{\rm max}$	$\log \mathcal{B}$	$\log \mathcal{L}_{\rm max}$	$\log \mathcal{B}$	$\log \mathcal{L}_{\rm max}$	$\log \mathcal{B}$	$\log \mathcal{L}_{\rm max}$	$\log \mathcal{B}$	$\log \mathcal{L}_{\rm max}$	$\log \mathcal{B}$	$\log \mathcal{L}_{\rm max}$
Ψ_4	Ψ_4	94.1	123.2	477.2	514.3	2033.7	2063.8	90.0	124.2	475.9	517.8	2042.7	2074.4
Ψ_4	$\delta^2 h_{\rm NF}$	93.9	123.2	477.0	514.4	2033.4	2063.7	89.9	124.0	475.7	517.6	2041.7	2073.4
$\delta^2 h_{\rm NF}$	$\delta^2 h_{\rm NF}$	93.8	123.1	476.5	513.7	2030.8	2061.3	89.2	123.9	475.0	516.8	2038.1	2070.1
$h_{\rm NF}$	$h_{\rm NF}$	93.6	123.8	476.5	513.7	2031.0	2061.3	89.2	123.1	474.5	516.8	2038.3	2070.1
Ψ_4	$\delta^2 h_{\rm F}$	93.6	122.9	475.7	512.7	2027.0	2057.3	83.9	117.8	451.0	492.3	1940.5	1971.9
$\delta^2 h_{\rm F}$	$\delta^2 h_{\rm F}$	92.4	121.5	470.7	507.3	2005.1	2035.5	64.1	98.2	372.7	414.1	1634.5	1665.8
$h_{\rm F}$	$h_{\rm F}$	92.2	121.5	470.1	507.3	2005.3	2035.5	64.1	98.3	372.7	414.1	1634.1	1665.7

$(\delta^2 h_{\mathrm{F/NF}})(t)$ and $h_{\mathrm{F/NF}}(t)$ should be exactly equal, modulo the uncertainty associated to the sampling of the likelihood throughout the parameter space. In fact, Table I shows that the evidences obtained by such pairs of analyses differ at most by 0.5 (which would not impact our conclusions regarding model selection), even in the highest SNR cases where convergence is harder to achieve, with most cases ranging between 0 and 0.2.

When sampling the likelihood, we fix the mass ratio and spins of the templates to those of the injection and sampling only over the total redshifted mass of the source M_{total}, the luminosity distance d_{L}, and orientation angles (ι, φ), the sky-location angles (α, δ), the polarization angle ψ, and the time of arrival. The power spectral densities used for our two injections are those of the Advanced LIGO and Virgo detectors at the times of GW190521 and S200114f. When analyzing the corresponding Ψ_4 or $\delta^2 h$ injections, we applied the correction factor in Eq. (11) to obtain the appropriate PSDs. We sample the parameter space using the nested sampler DYNESTY [130] with 4096 live points for the cases with SNR $= 15$ and 30, and 8192 live points for the cases with SNR $= 60$.

C. Results on simulated signals

Table I shows the natural log Bayes factor ($\log \mathcal{B}$) and the maximum log-likelihood ($\log \mathcal{L}_{\mathrm{max}}$) recovered by each of our analyses for each of our two types of injections. First, we note that in both cases, the analyses making use of strain waveforms $h_{\mathrm{F(NF)}}$ and the corresponding second-order finite-differenced waveforms $\delta^2 h_{\mathrm{F(NF)}}$ yield equivalent results even for SNRs of 60, corroborating that our formalism does not introduce any artifacts. This means there is no fundamental reason to prefer an analysis based on strain. Therefore, given that the Ψ_4 waveforms, directly obtained from ψ_4, avoid a complete layer of systematic errors, in the following we use the results based on the injection and recovery of Ψ_4 itself as our reference results. Since we checked above that sampling errors introduce maximal uncertainties in the Bayes factors of $\simeq 0.5$ (irrelevant for the purpose of model selection), we will assume that any significant difference between our reference analysis and the remaining ones is due to artifacts arising from the integration of $\psi_4(t)$ to obtain $h(t)$.

Figure 6 shows posterior parameter distributions for all injection-template combinations in Table I, for the case of

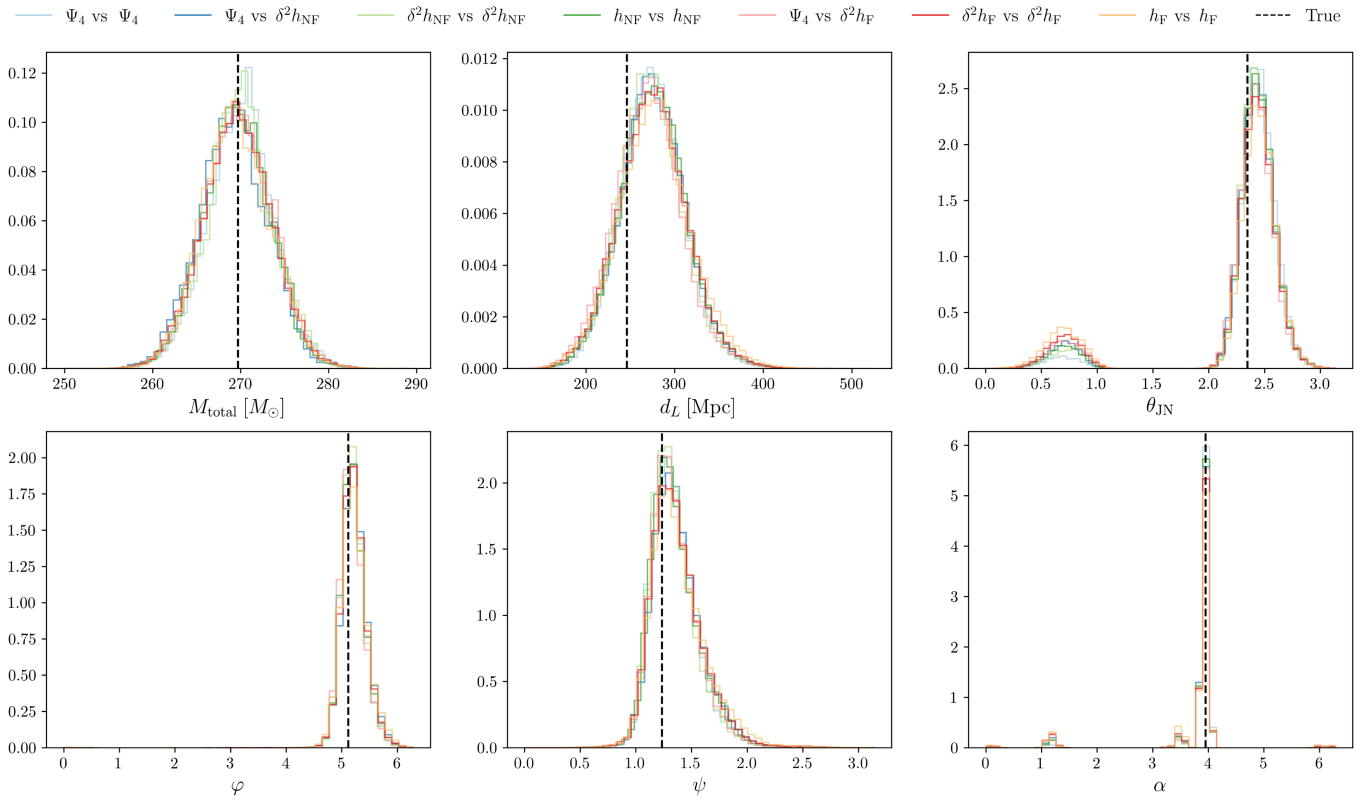

FIG. 6. Posterior parameter distributions for our GW190521-like injection, when scaled to a signal-to-noise ratio of 15. Posterior parameter distributions for our different analyses in Table I together with the true value represented by a dashed line. The color code denotes the type of injection used [Ψ_4, strain $h(t)$, or strain-derived Ψ_4 denoted by $\delta^2 h(t)$] and the type of template. All analyses yield equivalent results. In particular, no significant difference is observed when filtered or nonfiltered injections and templates are used. The parameter θ_{JN} describes the angle formed between the total angular momentum of the source and the line of sight. We note that since our sources do not precess, this is equal to the parameter ι.

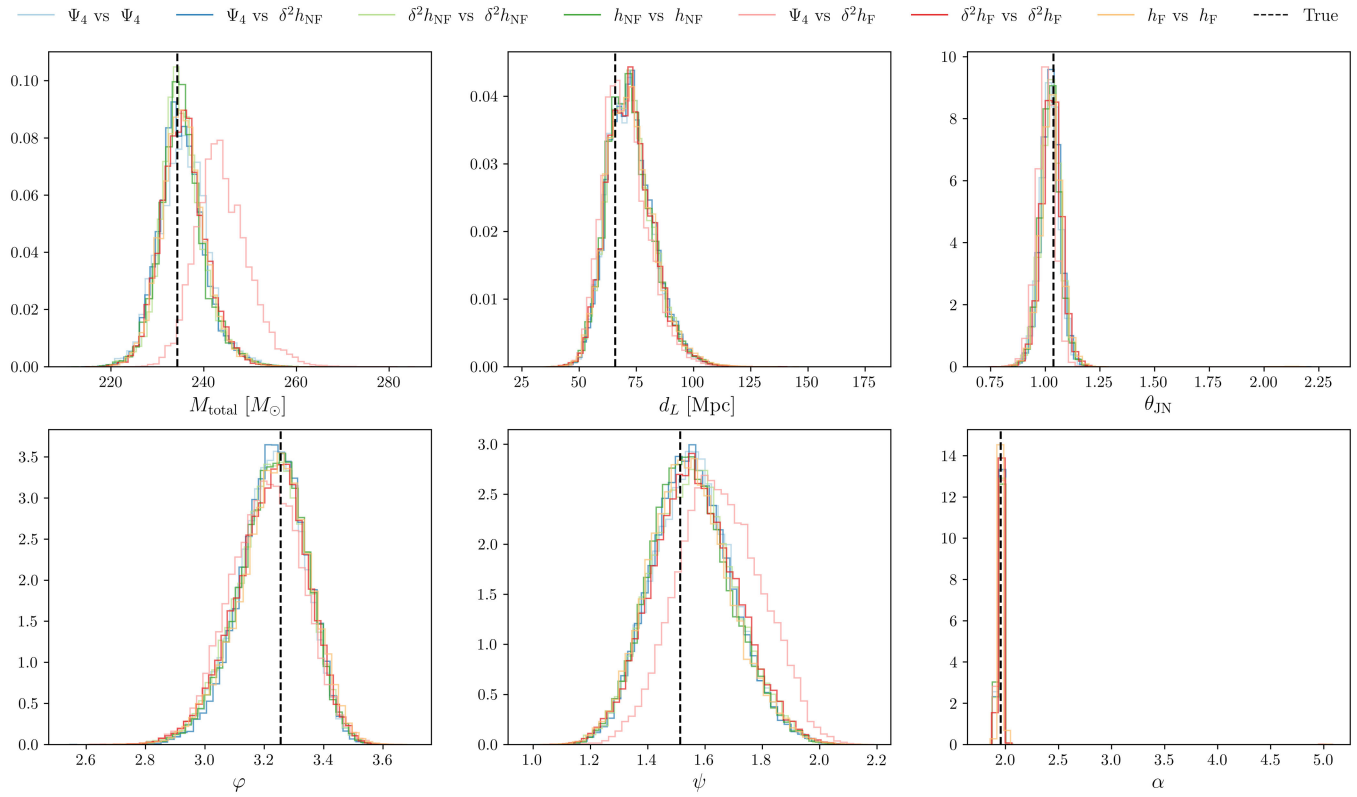

FIG. 7. Posterior parameter distributions for our S200114f-like injection, when scaled to a signal-to-noise ratio of 15. Posterior parameter distributions for our different analyses in Table I together with the true value represented by a dashed line. The color code denotes the type of injection used [Ψ_4, strain $h(t)$, or strain-derived $\Psi_4 \equiv (\delta^2 h)(t)$] and the type of template. Recovering nonfiltered injections with filtered waveforms leads to visible shifts in some posteriors. This is due to the excessive aggressiveness of the integration filter.

our GW190521-like signal scaled to an SNR of 15. The vertical bars show the true injection values. Similarly, Fig. 7 shows the same for our S200114f-like injection. In the first case, all distributions yield equivalent results. In particular, since our choice of ω_0 barely affects the signal morphology, there is no significant difference between the posteriors obtained when injecting either $\Psi_4(t)$, $h_{\rm F}(t)$, or $h_{\rm NF}(t)$ and recovering with any of the relevant template models. We find the same is true when we raise the SNR to 30 and 60. In particular, the top contours of Fig. 8 show the symmetric 90% credible intervals around the median obtained for the total mass as a function of the SNR of the Ψ_4 injection when this is recovered with Ψ_4 itself (blue) and $\delta h_{\rm F}^2$, which carries potential integration and ω_0-choice artifacts. Both these contours are essentially equal and converge to the true value for increasing SNR, indicating that, in this case, the aforementioned artifacts are mild enough to not bias parameter estimation. However, the likelihoods reported in Table I and in the left-hand panel of Fig. 9 show that the runs involving injections [$h_{\rm F}(t)$ and $(\delta^2 h_{\rm F})(t)$] reach slightly lower log-likelihoods due to the (small) power eliminated by the choice of ω_0, which reduces the SNR of the injection. Nevertheless, as Table I shows, for the cases with SNR $= 15$ and 30 such missing power does not cause changes in the Bayes factors that can lead to qualitatively different conclusions when performing model selection. Accordingly, we will later show that the analysis of GW190521 is not impacted at all by the usage of $h_{\rm F}$ templates. This is, however, not the case when the SNR is raised to 60. In this situation, while parameter estimation is unaffected, we observe that analyzing a true GW with our filtered waveforms causes a drop of $\simeq 6$ in the Bayesian evidence, sufficient to lead to model selection biases.

The situation is quite different for the case of our second injection. In this case, the choice of ω_0 does significantly affect both the morphology and signal power of the waveform. As a consequence, Fig. 7 shows clear shifts of the posteriors for the total mass and the polarization angle when we recover the Ψ_4 injection with the $\delta^2 h_{\rm F}$ templates at an SNR of only 15, even if these are not completely inconsistent with the others. Figure 8 shows, however, that such shifts bias the estimate of the total mass when the SNR is above 30. This turns even more dramatic when evaluating the impact on the recovered log-likelihood and on model selection. The yellow distribution in the right-hand panel of Fig. 9 shows that the "F" templates [e.g., $(\delta^2 h_{\rm F})$] fail to recover a significant amount of power

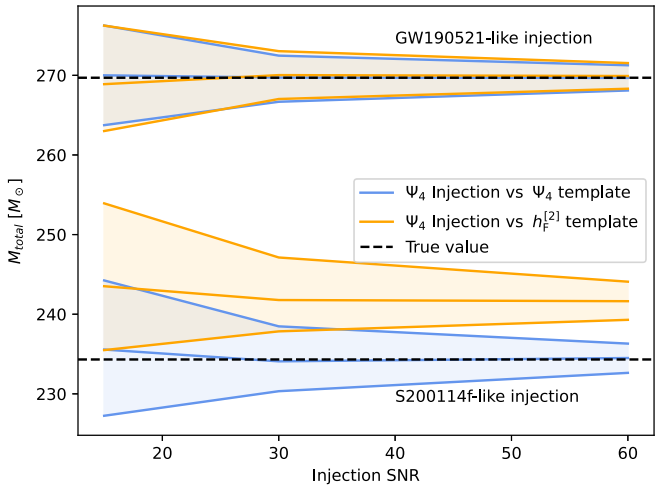

FIG. 8. Total mass bias due to ψ_4 integration and filtering as function of signal loudness. The blue and orange contours denote the 90% credible intervals for the total mass for the case of our GW190521-like and S200114f-like injections as a function of the injection signal-to-noise ratio. The injection is always modeled by Ψ_4, free of integration errors. The blue and orange contours denote, respectively, the result of analyzing the injection with Ψ_4 itself and with the $(\delta^2 h_F)$, which inherits the ψ_4-integration errors together with the power loss due to the choice of an integration low-frequency cutoff ω_0.

from Ψ_4, therefore dramatically reducing the maximum log-likelihood. This leads to a significant drop in the Bayes factor, as shown in Table I, that can change qualitative conclusions concerning model selection even when the SNR is only of 15. In fact, as we will show later, using h_F templates has strong consequences for the analysis of S200114f. Finally, as expected, injecting any of the "F" waveforms leads to a significant drop in the power present in the injection and, therefore, in the recovered power and Bayes factor.

VII. RESULTS ON REAL DATA I: GW190521 AS A BOSON-STAR MERGER

We now demonstrate our framework on real GW data. In Ref. [64] we performed parameter estimation and model selection on 4 sec of data around the time of GW190521, comparing this event to a "vanilla" quasicircular BBH model employed by the LIGO-Virgo-KAGRA (LVK) Collaboration [131] and to a set of numerical simulations for Proca-star mergers. Here we reproduce this analysis both using the classical strain formalism and our new ψ_4-based framework. We obtain our Ψ_4 input data by applying the transformations in Eqs. (4) and (11) to the public strain data and the corresponding strain PSDs.

We compare GW190521 to a family of numerical simulations for head-on mergers of Proca stars with equal mass and spin. The spin of the Proca stars can be directly mapped onto the bosonic field frequency, which is uniformly distributed in $\omega/\mu_B \in [0.80, 0.93]$ with a resolution of $\Delta\omega/\mu_B = 0.0025$. In addition, as in Ref. [64], we use a secondary exploratory family of unequal-mass mergers in which the frequency of one of the stars is fixed to $\omega_1/\mu_B = 0.895$ and the other varies uniformly in $\omega_2/\mu_B \in [0.80, 0.93]$. We perform model selection with respect to the classical circular BBH case for which we choose the waveform model NRSur7dq4 [53] implemented in the LALSuite library [132]. This model includes all gravitational-wave modes with $\ell \leq 4$ and is directly calibrated to precessing NR simulations with mass ratio $q = m_1/m_2 \in [1, 4]$ and individual spin magnitudes $a_i \in [0, 0.8]$. Moreover, the model can be extrapolated to $q = 6$ and $a_i = 0.99$. In our original study [64], we made use of the parameter estimation software BILBY [28] and sampled the likelihood across the parameter space using nested sampler CPNest [133]. In this work, however, we switch to the parallelizable version of BILBY, known as PARALLEL BILBY [134], and the sampler DYNESTY [130]. Owing to this

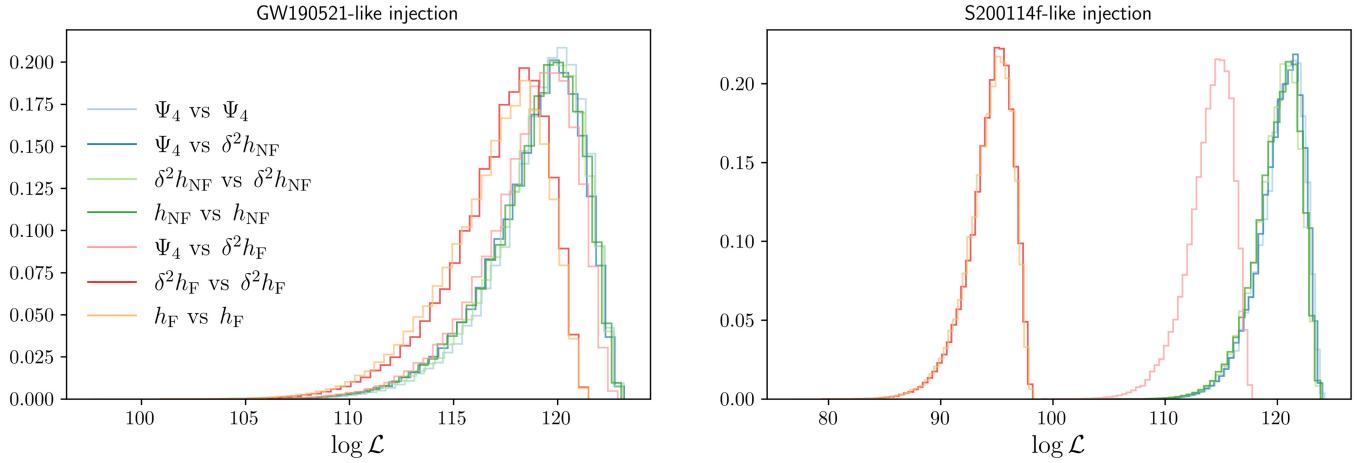

FIG. 9. Likelihood posterior distributions for our two sets of parameter inference runs. Left: posterior distributions for the case of our GW190521-like injections. Right: same for our S200114f-like injections.

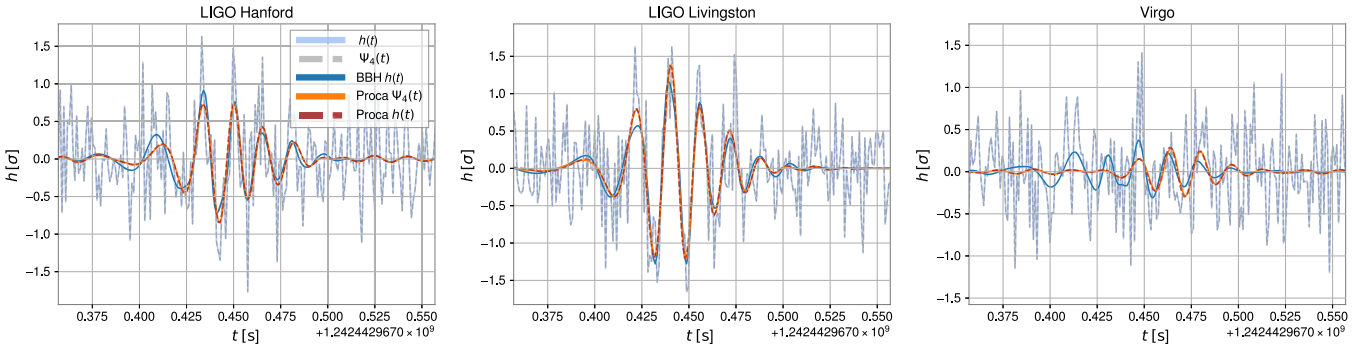

FIG. 10. Whitened detector data and maximum likelihood waveforms for GW190521. We show the whitened strain $h(t)$ (light blue) and $\Psi_4(t)$ (gray) detector data around the time of GW190521 together with the maximum likelihood waveforms returned by the BBH model NRSur7dq4 (blue) and by our equal-mass Proca-star merger simulations obtained through strain (brown) and $\Psi_4(t)$ analyses (orange).

change in software, we also repeat our original analysis based on strain data. We impose the same parameter priors as in Ref. [64], as detailed below.

Bayesian priors. For the intrinsic source parameters, we consider uniform priors on the field frequency $\omega/\mu_B \in [0.80, 0.93]$ and the total redshifted mass $M \in [50, 500] M_\odot$. For the extrinsic parameters, we impose a distance prior uniform in comoving volume with $d_L \in [10, 10000]$ Mpc, flat priors on the polarization angle and time of arrival, and isotropic priors on the source orientation and sky location. For the BBH model, we set identical priors in all of the parameters shared with the Proca-star merger (PSM) model. In addition, we set uniform priors on the dimensionless spin magnitudes and isotropic priors on their orientations. As in Ref. [64], we set a uniform prior on the mass ratio $q \in [1/6, 1]$. Finally, we note that as in Ref. [127], and as in the analysis of S200114f we describe later, we have tried an alternative prior uniform on the (inverse) mass ratio $Q \in [1, 6]$, and we have also tried to restrict the mass-ratio ranges to $Q \in [1, 4]$ and $q \in [1/4, 1]$. All of these yield evidences that differ, at most, by 0.2, therefore leading to identical conclusions regarding model selection.

A. Model selection

Figure 10 shows the whitened data of the Hanford, Livingston, and Virgo detectors at the time of GW190521, for both the case of $h(t)$ and $\Psi_4(t)$. Together, we overlay the maximum likelihood waveforms returned by the BBH model and by both our strain and ψ_4-based analyses when using our equal-mass Proca-star mergers. First, we note that the two latter analyses return essentially identical waveforms, once again showing that both analyses are equivalent modulo systematic errors coming from the obtention of $h(t)$.

Table II shows the natural logarithm of the Bayes factor ($\log \mathcal{B}$) for our different models under different choices of the distance prior. First, we note that for the same prior and waveform model, the Ψ_4 and strain analyses produce almost identical results. Second, consistently with Ref. [64], the first column shows that when attaching to the standard distance prior which is uniform in comoving volume, both the equal and unequal-mass models yield $\log \mathcal{B}$ only slightly larger than the BBH model. In particular, using Ψ_4 as our reference analysis, the equal (unequal-mass) model is $e^{0.8} \simeq 2$ ($e^{1.7} \simeq 5.5$) times more probable than the BBH model. The second column shows results obtained under the assumption of a uniform distance prior. Although this can be considered to be rather nonphysical, this prior effectively removes the intrinsic bias toward louder sources (as circular BBHs) that can be observed from much farther away than much weaker head-on mergers, which was induced by the previous prior. Alternatively, results obtained under the uniform prior can be considered as crude estimates of what would happen once numerical simulations for (intrinsically louder) less eccentric configurations of Proca-star mergers become available [135]. Once again, using our Ψ_4 analysis as a reference, the equal and unequal-mass models are favored with probabilities $e^{3.3} = 27:1$ and $e^{4.2} = 67:1$ with respect to the BBH case. These results are perfectly consistent with those obtained from the analysis of strain data and with those reported in Ref. [64].

TABLE II. Model selection for GW190521. We report the natural log Bayes factor obtained for our different waveform models. For the Proca-star merger model, analyses done under the classical strain formalism and our Ψ_4 formalism are equivalent.

	$\log \mathcal{B}$	
Waveform model	Comoving volume	Uniform
BBH (NRSur7dq4)	89.6	89.7
Proca $q = 1$ $h(t)$	90.6	93.2
Proca $q \neq 1$ $h(t)$	91.4	94.0
Proca $q = 1$ $\Psi_4(t)$	90.4	93.0
Proca $q \neq 1$ $\Psi_4(t)$	91.3	93.9

TABLE III. Parameters of GW190521 as a head-on Proca-star merger. We report median values together with symmetric 90% credible intervals under the scenario of an equal-mass, equal-spin merger and under our exploratory unequal-mass model. Columns labeled by $h(t)$ correspond to a "classical" analysis performed with strain data and templates, while those labeled by $\psi_4(t)$ make use of $\Psi_4(t)$ data and templates. We quote results corresponding to a distance prior uniform in comoving volume.

	Waveform model			
	$q=1$		$q\neq 1$	
Parameter	$h(t)$	$\psi_4(t)$	$h(t)$	$\psi_4(t)$
Total mass ($M_\odot$)	258^{+12}_{-10}	260^{+8}_{-9}	260^{+9}_{-10}	262^{+8}_{-7}
Total source-frame mass ($M_\odot$)	232^{+12}_{-17}	233^{+12}_{-16}	232^{+14}_{-15}	232^{+14}_{-15}
Primary source-frame mass ($M_\odot$)	116^{+6}_{-9}	117^{+5}_{-8}	120^{+10}_{-9}	120^{+9}_{-10}
Secondary source-frame mass ($M_\odot$)	116^{+6}_{-9}	117^{+5}_{-8}	111^{+8}_{-7}	111^{+8}_{-7}
Luminosity distance (Mpc)	541^{+305}_{-176}	544^{+296}_{-163}	592^{+358}_{-262}	618^{+360}_{-244}
Inclination (rad)	$0.83^{+0.23}_{-0.45}$	$0.85^{+0.23}_{-0.36}$	$0.67^{+0.36}_{-0.45}$	$0.67^{+0.33}_{-0.45}$
Final spin	$0.69^{+0.04}_{-0.04}$	$0.70^{+0.04}_{-0.03}$	$0.70^{+0.03}_{-0.05}$	$0.71^{+0.02}_{-0.05}$
Primary field frequency ω_1/μ_B	$0.890^{+0.018}_{-0.018}$	$0.895^{+0.015}_{-0.015}$	0.895	0.895
Secondary field frequency ω_2/μ_B	$0.890^{+0.018}_{-0.018}$	$0.895^{+0.015}_{-0.015}$	$0.900^{+0.018}_{-0.018}$	$0.905^{+0.015}_{-0.018}$
Boson mass $\mu_B(10^{-13}$ eV)	$8.80^{+0.76}_{-0.93}$	$8.60^{+0.63}_{-0.62}$	$8.63^{+0.70}_{-0.68}$	$8.57^{+0.64}_{-0.67}$

B. Parameter estimation

Table III shows our parameter estimates for GW190521. We report median values together with symmetric 90% credible intervals. The $q=1$ rows correspond to results obtained with our equal-mass simulations while the $q\neq 1$ rows correspond to those obtained with our exploratory unequal-mass simulations. For each of these, we report results from the analysis of both strain and Ψ_4 data.

First, we note that, as expected from the previous section, strain and Ψ_4 produce almost identical results. Consistent with Ref. [64], and taking Ψ_4 analysis using $q=1$ waveforms as a reference, we find that GW190521 can be interpreted as a head-on merger of two Proca stars with masses $117^{+5}_{-8}M_\odot$ that left behind a black hole with a final mass of $M_f=233^{+12}_{-16}M_\odot$ and spin of $a_f=0.70^{+0.04}_{-0.03}$, observed at a distance of 544^{+296}_{-163} Mpc. Because of the much lower intrinsic loudness of head-on mergers, the inferred distance and total mass are in large contrast with those inferred by the LVK Collaboration, respectively, $\simeq$5 Gpc and $\simeq 150M_\odot$. For the Proca stars, we infer a field frequency $\omega/\mu_B=0.895^{+0.15}_{-0.15}$. Combined with the total mass, this yields an ultralight boson mass of $8.60^{+0.63}_{-0.62}\times 10^{-13}$ eV. Our analysis making use of unequal-mass stars yields consistent conclusions. In particular, it yields a boson mass of $8.57^{+0.64}_{-0.67}\times 10^{-13}$ eV.

VIII. RESULTS ON REAL DATA II: THE TRIGGER S200114f

Finally, we show a real data example for which our framework makes an important difference. The trigger S200114f is a LIGO-Virgo high-mass trigger detected by a model agnostic search that identifies coherent excess power across the detector network, known as coherent WaveBurst [136], with a highly significant false-alarm rate of 1/17 yr [128]. This trigger has, however, challenged existing waveform models. In particular, while the LVK Collaboration analyzed S200114f under three BBH waveform models, no pair of these models returned consistent parameter estimates. Far from indicating that this trigger is not of astrophysical origin, this a symptom that the mentioned waveform models disagree in the regions of the parameter space where they best reproduce the signal. However, this trigger is morphologically consistent with a type of noise transients known as Tomte glitches [137]. In this situation, the LVK decided not to classify it as a confident or cataloged detection but, importantly, nor was it classified as a noise trigger.

The above characteristics make S200114f a tantalizing candidate to compare to our simulation catalog of Proca-star mergers, in the same way we previously treated GW190521. We note, however, that because we find that S200114f was poorly reproduced by the small simulation sets mentioned above, here we use an enhanced bank of nearly 759 simulations spanning a grid across the two-dimensional space defined by the field-oscillation frequencies of the two stars, which range in $\omega_{1,2}/\mu_B\in[0.80,0.93]$. Because of this enhancement, we use priors that slightly differ from those of the GW190521 analysis, which we specify below. Just as for the case of GW190521, we perform our comparison to the BBH model NRSur7dq4 within the strain framework while for the Proca-star case we use both the strain and Ψ_4 formalisms. Unlike in the

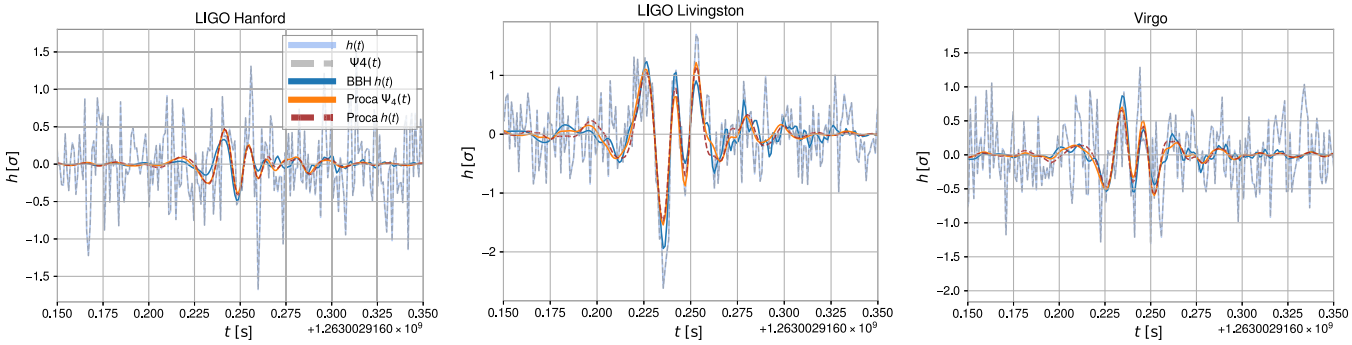

FIG. 11. Whitened detector data and maximum likelihood waveforms for S200114f. We show the whitened strain $h(t)$ (light blue) and $\Psi_4(t)$ (gray) detector data around the time of GW190521 together with the maximum likelihood waveforms returned by the BBH model NRSur7dq4 (blue) and by our equal-mass Proca-star merger simulations obtained through strain (brown) and $\Psi_4(t)$ analyses (orange). Unlike in Fig. 9 for the case of GW190521, in this case, the brown and orange waveforms show visible differences particularly visible in the early part of the waveforms. These translate into a worse fit to the data in the brown case and qualitatively different conclusions in terms of model selection.

case of GW190521, however, we find that both methods return significantly different results that arise from the fact that integration or filtering issues affect the best-fitting strain waveforms.

Bayesian priors. For the PSM model, we impose the same priors as in our GW190521 study, with the exception of the field frequencies. For these, we impose a prior uniform across the triangle defined by $\omega_{1,2}/\mu_B \in [0.80, 0.93]$, with $\omega_1/\mu_B \geq \omega_2/\mu_B$. Finally, for the BBH model, we impose the same priors as for the GW190521 case. However, from the four mass-ratio priors we discuss we retain the one yielding the largest Bayesian evidence for the Ψ_4 run. The goal of this is to be as conservative as we can in our statements in favor of the existence of Proca stars. These priors are identical to those imposed in Ref. [127], where we refer the reader to for further details.

A. Model selection

Figure 11 shows the whitened time series from the three detectors around the time of S200114f. Overlaid, we show the maximum likelihood waveforms for the BBH case and for the Proca-star merger case, the latter in terms of both strain and Ψ_4. Unlike for the case of GW190521, the latter two (brown and orange lines) clearly differ. This difference is particularly visible in the early premerger part of the signal, which is most prone to be affected by integration artifacts and choices of the integration frequency cutoff. Additional differences are also observable in the late ringdown part. While visually mild, such disagreement drives dramatically different values of the corresponding likelihood, which is $6e$-folds larger in the Ψ_4 case. This, in turn, has a great impact on model selection, as shown in Table IV. While under the Ψ_4 formalism we obtain $\log \mathcal{B} = 2.0$, this is reduced to $\log \mathcal{B} = -7.6$ when using strain templates, in the case where we use our distance prior uniform in comoving volume. In other words, while the trigger is slightly preferred as a Proca-star merger under the artifact-free Ψ_4 analysis, such an option is conclusively discarded under the strain analysis due to the artifacts arisen during the waveform integration process. We note that this result is qualitatively consistent with that returned by the noise-free injection study described in Sec. VI C. In particular, the $\log \mathcal{B}$ reported in the first (Ψ_4 vs Ψ_4) and fifth (Ψ_4 vs $\delta^2 h_F$) rows of the fourth column of Table I differ by 6.1 units, as compared to the 9.2 units we obtain in real data. Finally, a similarly dramatic effect is observed when we use a prior uniform in distance. In this case, the usage of strain waveforms causes a reduction from $\log \mathcal{B} = 5.3$ to $\log \mathcal{B} = -0.3$, i.e., from a strong preference for the Proca-star scenario to rather equal preference for both scenarios.

B. Parameter estimation

Finally, for the sake of completeness, Table V shows our parameter estimates for S200114f under both the strain and Ψ_4 analyses. First, clear differences arise in the estimated luminosity distance, total redshifted mass, star frequency, and spin parameters. These translate into biases in the boson mass and source-frame mass estimates. In particular, the boson-mass estimate from the strain formalism is highly consistent with that of GW190521 while it becomes highly inconsistent if using the integration-error-free Ψ_4 waveforms.

TABLE IV. Model selection for S200114f. We report the natural log Bayes factor obtained for our different waveform models under different signal models and distance priors.

	$\log \mathcal{B}$	
Waveform model	Comoving volume	Uniform
BBH (NRSur7dq4)	69.1	71.0
Proca $h(t)$	61.5	69.7
Proca $\Psi_4(t)$	71.1	76.3

TABLE V. Parameters of S200114f as a head-on Proca-star merger. We report median values together with symmetric 90% credible intervals. The column labelled by $h(t)$ corresponds to a "classical" analysis performed with strain-data and templates; while that labeled by $\psi_4(t)$ makes use of $\Psi_4(t)$-data and templates. We quote results obtained under a distance prior uniform in co-moving volume.

	Waveform model	
Parameter	$h(t)$	$\psi_4(t)$
Total mass $(M_\odot)$	233^{+15}_{-29}	215^{+18}_{-15}
Total source-frame mass $(M_\odot)$	228^{+17}_{-29}	207^{+16}_{-14}
Primary source-frame mass $(M_\odot)$	123^{+8}_{-14}	119^{+9}_{-14}
Secondary source-frame mass $(M_\odot)$	107^{+7}_{-17}	88^{+16}_{-7}
Luminosity distance (Mpc)	88^{+109}_{-28}	152^{+73}_{-61}
Inclination (rad)	$1.03^{+0.32}_{-0.45}$	$0.91^{+0.50}_{-0.24}$
Final spin	$0.63^{+0.07}_{-0.01}$	$0.66^{+0.03}_{-0.04}$
Primary field frequency ω_1/μ_B	$0.887^{+0.033}_{-0.019}$	$0.919^{+0.006}_{-0.043}$
Secondary field frequency ω_2/μ_B	$0.833^{+0.040}_{-0.025}$	$0.810^{+0.062}_{-0.010}$
Boson mass $\mu_B(10^{-13}$ eV)	$9.67^{+0.67}_{-0.49}$	$10.20^{+0.68}_{-0.55}$
$\log \mathcal{B}^{\text{Proca-star}}_{\text{BBH}}$	−7.6	2.0

IX. DISCUSSION OF RESULTS: INTEGRATED STRAIN VS NEWMAN-PENROSE SCALAR

Given our results, both on synthetic signals and on real data, the question arises of what is special about the waveforms reproducing S200114f that makes strain waveforms problematic, as opposed to the case of GW190521.

The answer is, nothing in principle. As stated throughout this paper, obtaining "integration-error-free" strain waveforms depends on a series of human choices (in particular that of ω_0) that are only reasonably well guided for the case of quasicircular mergers. In other cases, obtaining clean strain waveforms through FFI (if possible at all) involves a much more convoluted trial-and-error process. Moreover, we understand that in the absence of a "true" reference strain waveform, concluding that the obtained waveform is correct can only be done through the comparison to the Newman-Penrose waveform, similarly to what we do in the right-hand panels of Figs. 4 and 5.

In this situation, we can only make the *everything but scientific argument* that the integration choices that happened to work correctly for the waveforms best fitting GW190521 (making our results in Ref. [64] safe from integration artifacts) did not work for the waveforms best fitting S200114f. This is, at least partially, explained by the fact that our choice of $M\omega_0$ does remove more true signal power for S200114f than for the GW190521-like injection. In this situation, it could be argued that better strain waveforms may have been obtained if further exploration of ω_0 choices was performed, although there is no guarantee that this process would lead to a driftless waveform containing all the true signal power. In fact, FFI does by definition eliminate some true signal power even in quasicircular cases. In our view, this exactly exemplifies the huge advantage that the usage of the Newman-Penrose scalar has over that of the integrated strain: the resulting waveforms are "uniquely defined," with no choices to be made beyond those pertaining to the specific configuration of the numerical simulation itself.

X. CONCLUSIONS

Extracting the properties of GW sources requires accurate waveform templates that can be compared to detector data. NR provides the most precise way to obtain such templates and it is often the only way. Computing GW strain waveforms from ψ_4 outputted by NR simulations that can be compared to the strain detector data is a nontrivial process subject to well-known systematics that can impact the physical interpretation of the source. Moreover, easing these errors is a rather artisan process subject to human choices that are not always obvious or even well motivated depending on the considered type of source. This is particularly problematic for some of the most astrophysically interesting sources LIGO and Virgo are starting to observe, like precessing mergers [7,138], or may observe in the future observing runs, like eccentric mergers or dynamical captures, for which there is no monotonic relation between GW frequency and time. We note that, even in cases where such relation exists, typical systematic errors of ∼1% in amplitude will always exist. Moreover, these are in practice impossible to know because the true waveform is not known [68]. By taking second-order finite differences on the detector strain data, we have presented a data analysis framework that allows us to directly compare GW data to ψ_4, removing the need to extract the GW strain from numerical simulations and the associated systematic errors. We have shown that our framework is equivalent to the traditional strain one modulo the potential systematic errors present in the strain waveforms. Therefore, given that Ψ_4 waveforms have one less layer of systematic errors than strain waveforms, classical strain analyses will, at best, be as faithful as Ψ_4-based waveforms.

As a demonstration of our framework in real data analysis, we have first repeated our previous study comparing GW190521 to numerically simulated strain waveforms from Proca-star mergers presented in Ref. [64], but using the direct Ψ_4 outputted by our numerical simulations. We obtain results completely consistent with the original ones, which is indicative that our strain waveforms best fitting GW190521 suffered, at most, from mild integration errors that did not impact our original analysis. Second, we have analyzed the high-mass trigger S200114f using an enhanced catalog of Proca-star merger simulations reported in Ref. [127]. In this case, we find that the usage of strain waveforms—affected by integration errors—has a huge impact in the interpretation of this signal, yielding

conclusions that differ dramatically with respect to those obtained by using error-free Ψ_4 waveforms.

Our framework removes the need to obtain strain waveforms from numerical relativity simulations, removing a complete layer of systematic errors. We note that while we have focused on the case of short numerical relativity simulations with rather "exotic" dynamics, the integration errors worsen with increasing waveform length. In particular, this makes such errors particularly troublesome in the task of constructing hybrid numerical-relativity post-Newtonian waveforms [139] that are matched at early times [68].

While we have discussed our procedure under the prevalent scenario where the transverse-traceless gauge is considered, its application to alternative gauge-independent formulations [91] is, in principle, straightforward. Similarly, while we have demonstrated our framework in the context of parameter inference and model selection [140], this is trivially applicable to the case of actual matched-filter searches for GW signals [143–148]. Finally, we note that since LVK results have so far been obtained under the assumption of quasicircular mergers, we have no reason to believe such results may be affected by the errors we have discussed here.

We plan to publish and maintain our code to perform gravitational-wave data analysis using the Newman-Penrose scalar, within the software BILBY [28,134] at Ref. [149]. The analyzed LIGO-Virgo data and the corresponding power spectral densities, in their strain versions, are publicly available at the online Gravitational-Wave Open Science Center [150,151].

ACKNOWLEDGMENTS

This research has made use of data or software obtained from the Gravitational Wave Open Science Center, a service of LIGO Laboratory, the LIGO Scientific Collaboration, the Virgo Collaboration, and KAGRA. LIGO Laboratory and Advanced LIGO are funded by the U.S. National Science Foundation (NSF) as well as the Science and Technology Facilities Council (STFC) of the United Kingdom, the Max-Planck-Society (MPS), and the State of Niedersachsen/Germany for support of the construction of Advanced LIGO and construction and operation of the GEO600 detector. Additional support for Advanced LIGO was provided by the Australian Research Council. Virgo is funded, through the European Gravitational Observatory (EGO), by the French Centre National de Recherche Scientifique (CNRS), the Italian Istituto Nazionale di Fisica Nucleare (INFN), and the Dutch Nikhef, with contributions by institutions from Belgium, Germany, Greece, Hungary, Ireland, Japan, Monaco, Poland, Portugal, and Spain. K. A. G. R. A. is supported by Ministry of Education, Culture, Sports, Science and Technology (MEXT), Japan Society for the Promotion of Science (JSPS) in Japan; National Research Foundation (NRF) and Ministry of Science and ICT (MSIT) in Korea; Academia Sinica (AS) and National Science and Technology Council (NSTC) in Taiwan. J. C. B. is supported by a fellowship from "la Caixa" Foundation (No. 100010434) and from the European Union's Horizon 2020 research and innovation programme under the Marie Skłodowska-Curie Grant Agreement No. 847648. The fellowship code is LCF/BQ/PI20/11760016. J. C. B. is also supported by the Research Grant No. PID2020–118635 GB-I00 from the Spain-Ministerio de Ciencia e Innovación. K. C. acknowledges the MHRD, Government of India, for the fellowship support. J. A. F. is supported by the Spanish Agencia Estatal de Investigación (Grants No. PGC2018-095984-B-I00 and No. PID2021-125485NB-C21) and by the Generalitat Valenciana (PROMETEO/2019/071). This work is supported by the Center for Research and Development in Mathematics and Applications (CIDMA) through the Portuguese Foundation for Science and Technology (FCT—Fundação para a Ciência e a Tecnologia), Reference No. UIDB/04106/2020, and by national funds (OE), through FCT, I. P., in the scope of the framework contract foreseen in nos. 4, 5, and 6 of the article 23, of the Decree-Law 57/2016, changed by Law 57/2017. We also acknowledge support from the projects PTDC/FIS-OUT/28407/2017, CERN/FIS-PAR/0027/2019, PTDC/FIS-AST/3041/2020, CERN/FIS-PAR/0024/2021, and 2022.04560.PTDC. N. S.-G. is supported by the Spanish Ministerio de Universidades, through a María Zambrano grant (ZA21-031) with reference UP2021-044, funded within the European Union-Next Generation EU. This work has further been supported by the European Union's Horizon 2020 research and innovation (RISE) programme H2020-MSCA-RISE-2017 Grant No. FuNFiCO-777740 and by the European Horizon Europe staff exchange (SE) programme HORIZON-MSCA-2021-SE-01 Grant No. NewFunFiCO-101086251. We acknowledge the use of IUCAA LDG cluster Sarathi for the computational and numerical work. The authors acknowledge computational resources provided by the CIT cluster of the LIGO Laboratory and supported by National Science Foundation Grants No. PHY-0757058 and No. PHY0823459, and the support of the NSF CIT cluster for the provision of computational resources for our parameter inference runs. This material is based upon work supported by NSF's LIGO Laboratory which is a major facility fully funded by the National Science Foundation.

APPENDIX A: RELATION BETWEEN THE FOURIER TRANSFORM OF THE SECOND-ORDER DIFFERENCE AND THE SECOND DERIVATIVE OF A TIME SERIES

Theorem A.1. Given a continuous-time time series $x(t)$ where $t \in (0, T)$ of duration T and the sampled time series $x[m]$ of sampling interval Δt where $m = 0, 1, \ldots, M-1$,

i.e., $M\Delta t = T$, if the Fourier transform of the continuous-time time series and the discrete Fourier transform of the sampled time series are equivalent, i.e., $\tilde{x}(k\Delta f) = \tilde{x}[k]$, where

$$\tilde{x}(f) = \int_0^T x(t)e^{-i2\pi ft}dt, \tag{A1}$$

$$\tilde{x}[k] = \Delta t \sum_{m=0}^{M-1} x[m]e^{-i2\pi mk/M}, \tag{A2}$$

and $\Delta f = 1/T$, and the second derivative of $x(t)$ exists at every point in $(0, T)$, then the Fourier transform of the second derivative of $x(t)$ and the discrete Fourier transform of the second difference of $x[m]$ are related by

$$\widetilde{\delta^2 x}[k] = \frac{1-\cos(2\pi k\Delta f\Delta t)}{2\pi^2(k\Delta f\Delta t)^2}\widetilde{x''}(k\Delta f), \tag{A3}$$

where $x''(t)$ is the second derivative of $x(t)$, and $\delta^2 x[m]$ is the second difference of $x[m]$ defined by

$$\delta^2 x[m] = \frac{x[m+1]-2x[m]+x[m-1]}{(\Delta t)^2}. \tag{A4}$$

Proof. The Fourier transform of $x(t)$ and $x''(t)$ are related by

$$\widetilde{x''}(f) = -4\pi^2 f^2 \tilde{x}(f). \tag{A5}$$

The discrete Fourier transform of $x[m]$ and $(\delta^2 x)[m]$ are related by

$$\widetilde{(\delta^2 x)}[k] = \frac{2[\cos(2\pi k/M)-1]}{(\Delta t)^2}\tilde{x}[k]. \tag{A6}$$

If $\tilde{x}(k\Delta f) = \tilde{x}[k]$, from Eqs. (A5) and (A6), we have

$$\widetilde{\delta^2 x}[k] = \frac{1-\cos(2\pi k\Delta f\Delta t)}{2\pi^2(k\Delta f\Delta t)^2}\widetilde{x''}(k\Delta f). \tag{A7}$$

■

When assuming $\tilde{x}(k\Delta f) = \tilde{x}[k]$, it is important to note that aliasing and spectral leakage are intrinsic to discrete Fourier transforms. These issues also arise in "regular" GW data analysis when computing the discrete Fourier transform of strain data. Proper data windowing, such as employing a Tukey window as we do, mitigates these errors by tapering data to zero at the ends of the segment while preserving the GW signal segment. Importantly, our method does not introduce any new sources of systematic errors. Therefore, the errors discussed above are equivalent to those encountered in regular GW data analysis and are considered for the sake of rigor.

In this context, the discrete Fourier transform of the sampled time series closely approximates the Fourier transform of the continuous-time series, validating Eq. (A3). Nevertheless, accuracy depends on precise discrete Fourier transform usage, necessitating caution regarding aliasing and spectral leakage. Appropriate data windowing is essential when applying the discrete Fourier transform.

APPENDIX B: DISTRIBUTION OF SECOND-DIFFERENCED NOISE

Theorem B.1. Let $\boldsymbol{x} \in \mathbb{R}^M$ be a discrete-time Gaussian process such that the mean is $\mathbb{E}[\boldsymbol{x}] = \boldsymbol{\mu}$ and the covariance is $\mathbb{E}[(\boldsymbol{x}-\boldsymbol{\mu})(\boldsymbol{x}-\boldsymbol{\mu})^T] = \boldsymbol{\Sigma}$. Let $\delta^2\boldsymbol{x} \in \mathbb{R}^M$ be the second difference of $\boldsymbol{x}$ defined by

$$(\delta^2 x)[m] = \frac{x[m+1]-2x[m]+x[m-1]}{(\Delta t)^2}, \tag{B1}$$

where $x[m]$ is the mth element of $\boldsymbol{x}$, and $M > 2$ and Δt are, respectively, the total length and the sampling interval of the discrete-time process, respectively. A periodic boundary condition is imposed such that $x[0] = x[M]$ and $x[M+1] = x[1]$, then $\delta^2\boldsymbol{x}$ is a discrete-time Gaussian process with mean $\boldsymbol{\mu}_2 = \boldsymbol{T}\boldsymbol{\mu}$ and covariance $\boldsymbol{\Sigma}_2 = \boldsymbol{T}\boldsymbol{\Sigma}\boldsymbol{T}$, where $\boldsymbol{T}$ is a $M \times M$ matrix with entries $T_{j,j} = -2/(\Delta t)^2$, $T_{j,j+1} = T_{j,j-1} = 1/(\Delta t)^2$ with a periodic boundary condition imposed on the matrix index; i.e., index 0 implies index M and index $M+1$ implies index 1, and otherwise zero.

Proof. The probability density function of the discrete-time stationary Gaussian process is

$$p(\boldsymbol{x}) = \frac{1}{(2\pi)^{M/2}|\boldsymbol{\Sigma}|^{1/2}}\exp\left(-\frac{1}{2}(\boldsymbol{x}-\boldsymbol{\mu})^T\boldsymbol{\Sigma}^{-1}(\boldsymbol{x}-\boldsymbol{\mu})\right). \tag{B2}$$

The second difference of $\boldsymbol{x}$ can be regarded as a linear transformation of $\boldsymbol{x}$. Since

$$\begin{bmatrix}(\delta^2x)[1]\\(\delta^2x)[2]\\\vdots\\(\delta^2x)[M]\end{bmatrix} = \begin{bmatrix}\frac{1}{(\Delta t)^2}(x[2]-2x[1]+x[M])\\\frac{1}{(\Delta t)^2}(x[3]-2x[2]+x[1])\\\vdots\\\frac{1}{(\Delta t)^2}(x[1]-2x[M]+x[M-1])\end{bmatrix}$$
$$= \frac{1}{(\Delta t)^2}\begin{bmatrix}-2&1&0&\cdots&0&1\\1&-2&1&\cdots&0&0\\\vdots&\vdots&\vdots&\ddots&\vdots&\vdots\\1&0&0&\cdots&1&-2\end{bmatrix}\begin{bmatrix}x[1]\\x[2]\\\vdots\\x[M]\end{bmatrix}, \tag{B3}$$

we can write $\delta^2\boldsymbol{x} = \boldsymbol{T}\boldsymbol{x}$, where

$$\boldsymbol{T} = \frac{1}{(\Delta t)^2}\begin{bmatrix} -2 & 1 & 0 & \cdots & 0 & 1 \\ 1 & -2 & 1 & \cdots & 0 & 0 \\ \vdots & \vdots & \vdots & \ddots & \vdots & \vdots \\ 1 & 0 & 0 & \cdots & 1 & -2 \end{bmatrix}, \tag{B4}$$

or $T_{j,j} = -2/(\Delta t)^2$, $T_{j,j+1} = T_{j,j-1} = 1/(\Delta t)^2$, and a periodic boundary condition is imposed on the matrix index; i.e., index 0 implies index N and index $N+1$ implies index 1, and otherwise zero. The probability density function of $\delta^2\boldsymbol{x}$ is then

$$\begin{aligned} q(\delta^2\boldsymbol{x}) &= p(\boldsymbol{T}^{-1}\delta^2\boldsymbol{x})\left|\frac{\partial(\boldsymbol{T}^{-1}\delta^2\boldsymbol{x})}{\partial(\delta^2\boldsymbol{x})}\right| \\ &= p(\boldsymbol{T}^{-1}\delta^2\boldsymbol{x})|\boldsymbol{T}^{-1}| \\ &= \frac{1}{|\boldsymbol{T}|}\frac{1}{(2\pi)^{M/2}|\boldsymbol{\Sigma}|^{1/2}}\exp\left(-\frac{1}{2}(\boldsymbol{T}^{-1}\delta^2\boldsymbol{x}-\boldsymbol{\mu})^T\boldsymbol{\Sigma}^{-1}(\boldsymbol{T}^{-1}\delta^2\boldsymbol{x}-\boldsymbol{\mu})\right) \\ &= \frac{1}{(2\pi)^{M/2}|\boldsymbol{T}\boldsymbol{\Sigma}\boldsymbol{T}|^{1/2}}\exp\left(-\frac{1}{2}(\mathbf{T}^{-1}\delta^2\boldsymbol{x}-\boldsymbol{\mu})^T\boldsymbol{\Sigma}^{-1}(\boldsymbol{T}^{-1}\delta^2\boldsymbol{x}-\boldsymbol{\mu})\right) \\ &= \frac{1}{(2\pi)^{M/2}|\boldsymbol{T}\boldsymbol{\Sigma}\boldsymbol{T}|^{1/2}}\exp\left(-\frac{1}{2}(\delta^2\boldsymbol{x}-\boldsymbol{T}\boldsymbol{\mu})^T(\boldsymbol{T}^{-1})^T\boldsymbol{\Sigma}^{-1}\boldsymbol{T}^{-1}(\delta^2\boldsymbol{x}-\boldsymbol{T}\boldsymbol{\mu})\right) \\ &= \frac{1}{(2\pi)^{M/2}|\boldsymbol{T}\boldsymbol{\Sigma}\boldsymbol{T}|^{1/2}}\exp\left(-\frac{1}{2}(\delta^2\boldsymbol{x}-\boldsymbol{T}\boldsymbol{\mu})^T(\boldsymbol{T}\boldsymbol{\Sigma}\boldsymbol{T}^T)^{-1}(\delta^2\boldsymbol{x}-\boldsymbol{T}\boldsymbol{\mu})\right) \\ &= \frac{1}{(2\pi)^{M/2}|\mathbf{T}\boldsymbol{\Sigma}\mathbf{T}|^{1/2}}\exp\left(-\frac{1}{2}(\delta^2\boldsymbol{x}-\boldsymbol{T}\boldsymbol{\mu})^T(\boldsymbol{T}\boldsymbol{\Sigma}\boldsymbol{T})^{-1}(\delta^2\boldsymbol{x}-\boldsymbol{T}\boldsymbol{\mu})\right), \end{aligned} \tag{B5}$$

where we have used $\boldsymbol{T}^T = \boldsymbol{T}$ since $\boldsymbol{T}$ is a symmetric matrix. Therefore, $\delta^2\boldsymbol{x}$ is a discrete-time Gaussian process with mean $\boldsymbol{T}\boldsymbol{\mu}$ and covariance $\boldsymbol{T}\boldsymbol{\Sigma}\boldsymbol{T}$. ∎

Lemma B.2. Let $\boldsymbol{x} \in \mathbb{R}^M$ be a stationary discrete-time Gaussian process such that the mean of each discrete point is $\mathbb{E}[x[m]] = \mu$ and the autocovariance is $K_{XX}[\tau] = \mathbb{E}[(x[m]-\mu)(x[m+\tau]-\mu)]$, then $\delta^2\boldsymbol{x}$ is also a stationary discrete-time Gaussian process with mean $\boldsymbol{\mu}_2 = \mathbf{0}$ and autocovariance $K_{XX}[\tau]$:

$$K_{XX,2}[\tau] = \frac{1}{(\Delta t)^4}(6K_{XX}[\tau] - 4K_{XX}[\tau-1] + K_{XX}[\tau-2] - 4K_{XX}[\tau+1] + K_{XX}[\tau+2]). \tag{B6}$$

The power spectral density $S_2[k]$ of $\delta^2\boldsymbol{x}$ is related to the power spectral density $S[k]$ of $\boldsymbol{x}$ by

$$S_2[k] = \frac{1}{(\Delta t)^4}\left[6 - 8\cos\left(\frac{2\pi k}{M}\right) + 2\cos\left(\frac{4\pi k}{M}\right)\right]S[k]. \tag{B7}$$

Proof. By Theorem B.1, $\delta^2\boldsymbol{x}$ is a discrete-time Gaussian process with mean $\boldsymbol{\mu}_2 = \boldsymbol{T}\boldsymbol{\mu}$ and covariance $\boldsymbol{\Sigma}_2 = \boldsymbol{T}\boldsymbol{\Sigma}\boldsymbol{T}$. The mean of $\delta^2\boldsymbol{x}$ is then

$$\boldsymbol{\mu}_2 = \boldsymbol{T}\boldsymbol{\mu} = \frac{1}{(\Delta t)^2}\begin{bmatrix} \mu - 2\mu + \mu \\ \mu - 2\mu + \mu \\ \vdots \\ \mu - 2\mu + \mu \end{bmatrix} = \mathbf{0}. \tag{B8}$$

The covariance matrix is

$$\begin{aligned}\Sigma_{2(n,m)} &= \sum_{k,l=1}^{N} T_{n,k}\Sigma_{k,l}T_{l,m} \\ &= \frac{1}{(\Delta t)^2}\sum_{l=1}^{N}(\Sigma_{n-1,l} - 2\Sigma_{n,l} + \Sigma_{n+1,l})T_{l,m} \\ &= \frac{1}{(\Delta t)^4}[(\Sigma_{n-1,m-1} - 2\Sigma_{n-1,m} + \Sigma_{n-1,m+1}) - 2(\Sigma_{n,m-1} - 2\Sigma_{n,m} + \Sigma_{n,m+1}) + (\Sigma_{n+1,m-1} - 2\Sigma_{n+1,m} + \Sigma_{n+1,m+1})] \\ &= \frac{1}{(\Delta t)^4}(6K_{XX}[|n-m|] - 4K_{XX}[|n-m-1|] + K_{XX}[|n-m-2|] - 4K_{XX}[|n-m+1|] + K_{XX}[|n-m+2|]),\end{aligned} \tag{B9}$$

which depends on the time difference only. $\delta^2\boldsymbol{x}$ is therefore also a stationary discrete-time Gaussian process. The autocovariance of $\delta^2\boldsymbol{x}$ is therefore

$$K_{XX,2}(\tau) = \frac{1}{(\Delta t)^4}(6K_{XX}[\tau] - 4K_{XX}[\tau-1] + K_{XX}[\tau-2] - 4K_{XX}[\tau+1] + K_{XX}[\tau+2]). \tag{B10}$$

Since the power spectral density $S[k]$ is related to the autocorrelation function $R_{XX}[m]$ by

$$S[k] = \sum_{m=1}^{M} R_{XX}[m]e^{-i2\pi mk/M}, \tag{B11}$$

the power spectral density of the stochastic process $\delta^2\boldsymbol{x}$ is therefore

$$\begin{aligned}S_2[k] &= \sum_{m=1}^{M} R_{XX,2}[m]e^{-i2\pi mk/M} \\ &= \sum_{m=1}^{M}(K_{XX,2}[m] + \mu_2\mu_2)e^{-i2\pi mk/M} \\ &= \sum_{m=1}^{M} K_{XX,2}[m]e^{-i2\pi mk/M} \\ &= \frac{1}{(\Delta t)^4}\sum_{m=1}^{M}(6K_{XX}[m] - 4K_{XX}[m-1] + K_{XX}[m-2] - 4K_{XX}[m+1] + K_{XX}[m+2])e^{-i2\pi mk/M} \\ &= \frac{1}{(\Delta t)^4}(6S[k] - 4S[k]e^{-i2\pi k/M} + S[k]e^{-i4\pi k/M} - 4S[k]e^{i2\pi k/M} + S[k]e^{i4\pi k/M}) \\ &= \frac{1}{(\Delta t)^4}[6 - 8\cos(2\pi k/M) + 2\cos(4\pi k/M)]S[k],\end{aligned} \tag{B12}$$

where $S[k]$ is the power spectral density of the stochastic process $\boldsymbol{x}$. ∎

APPENDIX C: PARAMETERS OF SIMULATED SIGNALS

Table VI shows the parameters of the two injections discussed in Sec. VI.

TABLE VI. Parameters of the synthetic signals analyzed in Sec. VI C. We quote the inclination in terms of the angle between the line of sight and the total angular momentum $\theta_{\rm JN}$ as well as the azimuthal angle of the observer φ (see Appendix I in Ref. [64]).

Parameter	GW190521	S200114f
Total redshifted mass ($M_\odot$)	269.69	234.31
Inclination $\theta_{\rm JN}$ (rad)	2.34	1.04
Azimuth φ	5.11	3.26
Luminosity distance (Mpc)	246.10	65.71
Polarization ψ	1.23	1.51
Right ascension α	3.94	1.95
Declination δ	0.93	0.08
Primary field frequency $\omega_1/\mu_{\rm B}$	0.9000	0.8800
Secondary field frequency $\omega_2/\mu_{\rm B}$	0.8550	0.8325

[1] J Aasi *et al.*, *Advanced LIGO*, Classical Quantum Gravity **32**, 074001 (2015).

[2] B. P. Abbott *et al.* (LIGO Scientific Collaboration and Virgo Collaboration), *Observation of gravitational waves from a binary black hole merger*, Phys. Rev. Lett. **116**, 061102 (2016).

[3] F. Acernese *et al.* (Virgo Collaboration), *Advanced Virgo: A second-generation interferometric gravitational wave detector*, Classical Quantum Gravity **32**, 024001 (2015).

[4] T. Akutsu *et al.*, *Overview of KAGRA: Detector design and construction history*, arXiv:2005.05574.

[5] B. P. Abbott *et al.* (LIGO Scientific Collaboration and Virgo Collaboration), *GWTC-1: A gravitational-wave transient catalog of compact binary mergers observed by LIGO and Virgo during the first and second observing runs*, Phys. Rev. X **9**, 031040 (2019).

[6] R. Abbott *et al.* (LIGO Scientific Collaboration and Virgo Collaboration), *GWTC-2: Compact binary coalescences observed by LIGO and Virgo during the first half of the third observing run*, Phys. Rev. X **11**, 021053 (2021).

[7] R. Abbott *et al.*, *GWTC-3: Compact binary coalescences observed by LIGO and Virgo during the second part of the third observing run*, arXiv:2111.03606.

[8] B. P. Abbott *et al.* (LIGO Scientific Collaboration and Virgo Collaboration), *GW170817: Observation of gravitational waves from a binary neutron star inspiral*, Phys. Rev. Lett. **119**, 161101 (2017).

[9] R. Abbott *et al.*, *Population properties of compact objects from the second LIGO–Virgo gravitational-wave transient catalog*, Astrophys. J. Lett. **913**, L7 (2021).

[10] R. Abbott *et al.*, *The population of merging compact binaries inferred using gravitational waves through GWTC-3*, arXiv:2111.03634.

[11] R. Abbott *et al.* (LIGO Scientific Collaboration and Virgo Collaboration), *Tests of general relativity with binary black holes from the second LIGO-Virgo gravitational-wave transient catalog*, Phys. Rev. D **103**, 122002 (2021).

[12] R. Abbott *et al.*, *Tests of general relativity with GWTC-3*, arXiv:2112.06861.

[13] Juan Calderón Bustillo, Paul D. Lasky, and Eric Thrane, *Black-hole spectroscopy, the no-hair theorem, and GW150914: Kerr versus Occam*, Phys. Rev. D **103**, 024041 (2021).

[14] Gregorio Carullo, Walter Del Pozzo, and John Veitch, *Observational black hole spectroscopy: A time-domain multimode analysis of GW150914*, Phys. Rev. D **99**, 123029 (2019).

[15] Maximiliano Isi, Matthew Giesler, Will M. Farr, Mark A. Scheel, and Saul A. Teukolsky, *Testing the no-hair theorem with GW150914*, Phys. Rev. Lett. **123**, 111102 (2019).

[16] Matthew Giesler, Maximiliano Isi, Mark A. Scheel, and Saul A. Teukolsky, *Black hole ringdown: The importance of overtones*, Phys. Rev. X **9**, 041060 (2019).

[17] Abhirup Ghosh, Richard Brito, and Alessandra Buonanno, *Constraints on quasinormal-mode frequencies with LIGO-Virgo binary–black-hole observations*, Phys. Rev. D **103**, 124041 (2021).

[18] Sizheng Ma, Ling Sun, and Yanbei Chen, *Black hole spectroscopy by mode cleaning*, Phys. Rev. Lett. **130**, 141401 (2023).

[19] Sizheng Ma, Ling Sun, and Yanbei Chen, *Using rational filters to uncover the first ringdown overtone in GW150914*, Phys. Rev. D **107**, 084010 (2023).

[20] J. Calderón Bustillo, J. A. Clark, P. Laguna, and D. Shoemaker, *Tracking black hole kicks from gravitational wave observations*, Phys. Rev. Lett. **121**, 191102 (2018).

[21] Juan Calderón Bustillo, Chris Evans, James A. Clark, Grace Kim, Pablo Laguna, and Deirdre Shoemaker, *Post-merger chirps from binary black holes as probes of the final black-hole horizon*, Commun. Phys. **3**, 176 (2020).

[22] Vijay Varma, Sylvia Biscoveanu, Tousif Islam, Feroz H. Shaik, Carl-Johan Haster, Maximiliano Isi, Will M. Farr, Scott E. Field, and Salvatore Vitale, *Evidence of large recoil velocity from a black hole merger signal*, Phys. Rev. Lett. **128**, 191102 (2022).

[23] Parthapratim Mahapatra, Anuradha Gupta, Marc Favata, K. G. Arun, and B. S. Sathyaprakash, *Remnant black hole kicks and implications for hierarchical mergers*, Astrophys. J. Lett. **918**, L31 (2021).

[24] Juan Calderón Bustillo, Samson H. W. Leong, and Koustav Chandra, *GW190412: Measuring a black-hole recoil direction through higher-order gravitational-wave modes*, arXiv:2211.03465.

[25] L. A. Wainstein and V. D. Zubakov, *Extraction of signals from noise* (Prentice-Hall, Englewood Cliffs, NJ, 1962).

[26] Bruce Allen, Warren G. Anderson, Patrick R. Brady, Duncan A. Brown, and Jolien D. E. Creighton, *FINDCHIRP: An algorithm for detection of gravitational waves from inspiraling compact binaries*, Phys. Rev. D **85**, 122006 (2012).

[27] J. Veitch, V. Raymond, B. Farr, W. Farr, P. Graff, S. Vitale, B. Aylott, K. Blackburn, N. Christensen, M. Coughlin *et al.*, *Parameter estimation for compact binaries with ground-based gravitational-wave observations using the LALInference software library*, Phys. Rev. D **91**, 042003 (2015).

[28] Gregory Ashton *et al.*, *BILBY: A user-friendly Bayesian inference library for gravitational-wave astronomy*, Astrophys. J. Suppl. Ser. **241**, 27 (2019).

[29] B. P. Abbott *et al.* (LIGO Scientific Collaboration and Virgo Collaboration), *Properties of the binary black hole merger GW150914*, Phys. Rev. Lett. **116**, 241102 (2016).

[30] Luc Blanchet, *Gravitational radiation from post-Newtonian sources and inspiralling compact binaries*, Living Rev. Relativity **17**, 2 (2014).

[31] Thibault Damour, Bala R. Iyer, and B. S. Sathyaprakash, *A comparison of search templates for gravitational waves from binary inspiral*, Phys. Rev. D **63**, 044023 (2001).

[32] A. Buonanno and T. Damour, *Effective one-body approach to general relativistic two-body dynamics*, Phys. Rev. D **59**, 084006 (1999).

[33] Frans Pretorius, *Evolution of binary black hole spacetimes*, Phys. Rev. Lett. **95**, 121101 (2005).

[34] B. Brügmann, J. A. Gonzalez, M. Hannam, S. Husa, U. Sperhake, and W. Tichy, *Calibration of moving puncture simulations*, Phys. Rev. D **77**, 024027 (2008).

[35] Manuela Campanelli, C. O. Lousto, P. Marronetti, and Y. Zlochower, *Accurate evolutions of orbiting black-hole binaries without excision*, Phys. Rev. Lett. **96**, 111101 (2006).

[36] John G. Baker, Joan Centrella, Dae-Il Choi, Michael Koppitz, and James van Meter, *Gravitational-wave extraction from an inspiraling configuration of merging black holes*, Phys. Rev. Lett. **96**, 111102 (2006).

[37] M. Boyle, D, A. Brown, L. E. Kidder, A. H. Mroue, H. P. Pfeiffer, M. A. Scheel, G. B. Cook, and S. A. Teukolsky, *High-accuracy comparison of numerical relativity simulations with post-Newtonian expansions*, Phys. Rev. D **76**, 124038 (2007).

[38] Karan Jani, James Healy, James A. Clark, Lionel London, Pablo Laguna, and Deirdre Shoemaker, *Georgia Tech catalog of gravitational waveforms*, Classical Quantum Gravity **33**, 204001 (2016).

[39] James Healy and Carlos O. Lousto, *Third RIT binary black hole simulations catalog*, Phys. Rev. D **102**, 104018 (2020).

[40] Michael Boyle, Daniel Hemberger, Dante A. B. Iozzo, Geoffrey Lovelace, Serguei Ossokine, Harald P. Pfeiffer, Mark A. Scheel, Leo C. Stein, Charles J. Woodford, Aaron B. Zimmerman *et al.*, *The SXS Collaboration catalog of binary black hole simulations*, Classical Quantum Gravity **36**, 195006 (2019).

[41] Ian Hinder, Alessandra Buonanno, Michael Boyle, Zachariah B Etienne, James Healy, Nathan K Johnson-McDaniel, Alessandro Nagar, Hiroyuki Nakano *et al.*, *Error-analysis and comparison to analytical models of numerical waveforms produced by the NRAR Collaboration*, Classical Quantum Gravity **31**, 025012 (2014).

[42] Luis Lehner and Frans Pretorius, *Numerical relativity and astrophysics*, Annu. Rev. Astron. Astrophys. **52**, 661 (2014).

[43] Tim Dietrich, David Radice, Sebastiano Bernuzzi, Francesco Zappa, Albino Perego, Bernd Brügmann, Swami Vivekanandji Chaurasia, Reetika Dudi, Wolfgang Tichy, and Maximiliano Ujevic, *Core database of binary neutron star merger waveforms*, Classical Quantum Gravity **35**, 24LT01 (2018).

[44] Alejandra Gonzalez, Francesco Zappa, Matteo Breschi, Sebastiano Bernuzzi, David Radice, Ananya Adhikari, Alessandro Camilletti, Swami Vivekanandji Chaurasia, Georgios Doulis, Surendra Padamata, Alireza Rashti, Maximiliano Ujevic, Bernd Brügmann, William Cook, Tim Dietrich, Albino Perego, Amit Poudel, and Wolfgang Tichy, *Second release of the CoRe database of binary neutron star merger waveforms*, Classical Quantum Gravity **40**, 085011 (2023).

[45] Sebastian Khan, Sascha Husa, Mark Hannam, Frank Ohme, Michael Pürrer, Xisco Jiménez Forteza, and Alejandro Bohé, *Frequency-domain gravitational waves from nonprecessing black-hole binaries. II. A phenomenological model for the advanced detector era*, Phys. Rev. D **93**, 044007 (2016).

[46] Sascha Husa, Sebastian Khan, Mark Hannam, Michael Pürrer, Frank Ohme, Xisco Jiménez Forteza, and Alejandro Bohé, *Frequency-domain gravitational waves from nonprecessing black-hole binaries. I. New numerical waveforms and anatomy of the signal*, Phys. Rev. D **93**, 044006 (2016).

[47] G. Pratten, Cecilio García-Quirós, M. Colleoni, A. Ramos-Buades, H. Estellés, M. Mateu-Lucena, R. Jaume, M. Haney, D. Keitel, J. E. Thompson, and S. Husa, *Computationally efficient models for the dominant and subdominant harmonic modes of precessing binary black holes*, Phys. Rev. D **103**, 104056 (2021).

[48] Cecilio García-Quirós, Sascha Husa, Maite Mateu-Lucena, and Angela Borchers, *Accelerating the evaluation of inspiral–merger–ringdown waveforms with adapted grids*, Classical Quantum Gravity **38**, 015006 (2020).

[49] S. Khan, F. Ohme, K. Chatziioannou, and M. Hannam, *Including higher order multipoles in gravitational-wave models for precessing binary black holes*, Phys. Rev. D **101**, 024056 (2020).

[50] Serguei Ossokine, Alessandra Buonanno, Sylvain Marsat, Roberto Cotesta, Stanislav Babak, Tim Dietrich, Roland Haas, Ian Hinder, Harald P. Pfeiffer, Michael Pürrer, Charles J. Woodford, Michael Boyle, Lawrence E. Kidder, Mark A. Scheel, and Béla Szilágyi, *Multipolar effective-one-body waveforms for precessing binary black holes: Construction and validation*, Phys. Rev. D **102**, 044055 (2020).

[51] Rossella Gamba, Sarp Akçay, Sebastiano Bernuzzi, and Jake Williams, *Effective-one-body waveforms for precessing coalescing compact binaries with post-Newtonian twist*, Phys. Rev. D **106**, 024020 (2022).

[52] Jonathan Blackman, Scott E. Field, Mark A. Scheel, Chad R. Galley, Christian D. Ott, Michael Boyle, Lawrence E. Kidder, Harald P. Pfeiffer, and Béla Szilágyi, *Numerical relativity waveform surrogate model for generically precessing binary black hole mergers*, Phys. Rev. D **96**, 024058 (2017).

[53] Vijay Varma, Scott E. Field, Mark A. Scheel, Jonathan Blackman, Davide Gerosa, Leo C. Stein, Lawrence E. Kidder, and Harald P. Pfeiffer, *Surrogate models for precessing binary black hole simulations with unequal masses*, Phys. Rev. Res. **1**, 033015 (2019).

[54] Felipe F. Freitas, Carlos A. R. Herdeiro, António P. Morais, António Onofre, Roman Pasechnik, Eugen Radu, Nicolas Sanchis-Gual, and Rui Santos, *Generating gravitational waveform libraries of exotic compact binaries with deep learning*, arXiv:2203.01267.

[55] B. P. Abbott *et al.* (LIGO Scientific Collaboration and Virgo Collaboration), *Directly comparing GW150914 with numerical solutions of Einstein's equations for binary black hole coalescence*, Phys. Rev. D **94**, 064035 (2016).

[56] R. Abbott *et al.* (LIGO Scientific Collaboration and Virgo Collaboration), *Properties and astrophysical implications of the* $150M_{\odot}$ *binary black hole merger GW190521*, Astrophys. J. Lett. **900**, L13 (2020).

[57] J. Lange, R. O'Shaughnessy, M. Boyle, J. Calderón Bustillo, M. Campanelli, T. Chu, J. A. Clark, N. Demos, H. Fong, J. Healy *et al.*, *Parameter estimation method that directly compares gravitational wave observations to numerical relativity*, Phys. Rev. D **96**, 104041 (2017).

[58] V. Gayathri, J. Healy, J. Lange, B. O'Brien, M. Szczepańczyk, Imre Bartos, M. Campanelli, S. Klimenko, C. O. Lousto, and R. O'Shaughnessy, *Eccentricity estimate for black hole mergers with numerical relativity simulations*, Nat. Astron. **6**, 344 (2022).

[59] Benjamin Aylott *et al.*, *Testing gravitational-wave searches with numerical relativity waveforms: Results from the first numerical INJection analysis (NINJA) project*, Classical Quantum Gravity **26**, 165008 (2009).

[60] J Aasi *et al.*, *The NINJA-2 project: Detecting and characterizing gravitational waveforms modelled using numerical binary black hole simulations*, Classical Quantum Gravity **31**, 115004 (2014).

[61] K. Chandra, V. Gayathri, J. C. Bustillo, and A. Pai, *Numerical relativity injection analysis of signals from generically spinning intermediate mass black hole binaries in advanced LIGO data*, Phys. Rev. D **102**, 044035 (2020).

[62] Juan Calderón Bustillo, Nicolas Sanchis-Gual, Alejandro Torres-Forné, and José A. Font, *Confusing head-on collisions with precessing intermediate-mass binary black hole mergers*, Phys. Rev. Lett. **126**, 201101 (2021).

[63] A. R. Williamson, J. Lange, R. O'Shaughnessy, J. A. Clark, Prayush Kumar, J. Calderón Bustillo, and J. Veitch, *Systematic challenges for future gravitational wave measurements of precessing binary black holes*, Phys. Rev. D **96**, 124041 (2017).

[64] J. C. Bustillo, N. Sanchis-Gual, A. Torres-Forné, J. A. Font, A. Vajpeyi, R. Smith, C. Herdeiro, E. Radu, and S. H. W. Leong, *GW190521 as a merger of Proca stars: A potential new vector boson of* 8.7×10^{-13} eV, Phys. Rev. Lett. **126**, 081101 (2021).

[65] Ezra Newman and Roger Penrose, *An approach to gravitational radiation by a method of spin coefficients*, J. Math. Phys. **3**, 566 (1962).

[66] Manuela Campanelli and Carlos O. Lousto, *Second order gauge invariant gravitational perturbations of a Kerr black hole*, Phys. Rev. D **59**, 124022 (1999).

[67] Hermann Bondi, M. G. J. Van der Burg, and A. W. K. Metzner, *Gravitational waves in general relativity, VII. Waves from axi-symmetric isolated system*, Proc. R. Soc. A **269**, 21 (1962).

[68] Christian Reisswig and Denis Pollney, *Notes on the integration of numerical relativity waveforms*, Classical Quantum Gravity **28**, 195015 (2011).

[69] L. Santamaría, F. Ohme, P. Ajith, B. Brügmann, N. Dorband, M. Hannam, S. Husa, P. Mösta, D. Pollney, C. Reisswig, E. L. Robinson, J. Seiler, and B. Krishnan, *Matching post-Newtonian and numerical relativity waveforms: Systematic errors and a new phenomenological model for nonprecessing black hole binaries*, Phys. Rev. D **82**, 064016 (2010).

[70] Rossella Gamba, Matteo Breschi, Gregorio Carullo, Piero Rettegno, Simone Albanesi, Sebastiano Bernuzzi, and Alessandro Nagar, *GW190521: A dynamical capture of two black holes*, arXiv:2106.05575.

[71] N. Sanchis-Gual, C. Herdeiro, José A. Font, E. Radu, and F. Di Giovanni, *Head-on collisions and orbital mergers of Proca stars*, Phys. Rev. D **99**, 024017 (2019).

[72] H. Dimmelmeier, C. D. Ott, A. Marek, and H. Thomas Janka, *The gravitational wave burst signal from core collapse of rotating stars*, Phys. Rev. D **78**, 064056 (2008).

[73] Pablo Cerdá-Durán, Nicolas DeBrye, Miguel A. Aloy, José A. Font, and Martin Obergaulinger, *Gravitational wave signatures in black-hole-forming core collapse*, Astrophys. J. Lett. **779**, L18 (2013).

[74] Sherwood Richers, Christian D. Ott, Ernazar Abdikamalov, Evan O'Connor, and Chris Sullivan, *Equation of state effects on gravitational waves from rotating core collapse*, Phys. Rev. D **95**, 063019 (2017).

[75] Paul D. Lasky, Eric Thrane, Yuri Levin, Jonathan Blackman, and Yanbei Chen, *Detecting gravitational-wave memory with LIGO: Implications of GW150914*, Phys. Rev. Lett. **117**, 061102 (2016).

[76] Tullio Regge and John A. Wheeler, *Stability of a Schwarzschild singularity*, Phys. Rev. **108**, 1063 (1957).

[77] Frank J. Zerilli, *Gravitational field of a particle falling in a Schwarzschild geometry analyzed in tensor harmonics*, Phys. Rev. D **2**, 2141 (1970).

[78] Vincent Moncrief, *Gravitational perturbations of spherically symmetric systems. I. The exterior problem*, Ann. Phys. (N.Y.) (New York) **88**, 323 (1974).

[79] Michael Boyle and Abdul H. Mroue, *Extrapolating gravitational-wave data from numerical simulations*, Phys. Rev. D **80**, 124045 (2009).

[80] Nigel T. Bishop, Roberto Gómez, Luis Lehner, and Jeffrey Winicour, *Cauchy-characteristic extraction in numerical relativity*, Phys. Rev. D **54**, 6153 (1996).

[81] Jeffrey Winicour, *Characteristic evolution and matching*, Living Rev. Relativity **15**, 2 (2012).

[82] Nigel T. Bishop and Christian Reisswig, *The gravitational wave strain in the characteristic formalism of numerical relativity*, Gen. Relativ. Gravit. **46**, 1643 (2013).

[83] Denis Pollney, Christian Reisswig, Erik Schnetter, Nils Dorband, and Peter Diener, *High accuracy binary black hole simulations with an extended wave zone*, Phys. Rev. D **83**, 044045 (2011).

[84] Jordan Moxon, Mark A. Scheel, Saul A. Teukolsky, Nils Deppe, Nils Fischer, Francois Hébert, Lawrence E. Kidder, and William Throwe, *SpECTRE Cauchy-characteristic evolution system for rapid, precise waveform extraction*, Phys. Rev. D **107**, 064013 (2023).

[85] C. Reisswig, C. D. Ott, U. Sperhake, and E. Schnetter, *Gravitational wave extraction in simulations of rotating stellar core collapse*, Phys. Rev. D **83**, 064008 (2011).

[86] Roberto De Pietri, Alessandra Feo, Francesco Maione, and Frank Loffler, *Modeling equal and unequal mass binary*

neutron star mergers using public codes, Phys. Rev. D **93**, 064047 (2016).
[87] Thanasis Giannakopoulos, David Hilditch, and Miguel Zilhao, *Hyperbolicity of general relativity in Bondi-like gauges*, Phys. Rev. D **102**, 064035 (2020).
[88] Thanasis Giannakopoulos, Nigel T. Bishop, David Hilditch, Denis Pollney, and Miguel Zilhao, *Gauge structure of the Einstein field equations in Bondi-like coordinates*, Phys. Rev. D **105**, 084055 (2022).
[89] Thanasis Giannakopoulos, Nigel T. Bishop, David Hilditch, Denis Pollney, and Miguel Zilhão, *Numerical convergence of model Cauchy-characteristic extraction and matching*, arXiv:2306.13010.
[90] N. Bishop, R. Isaacson, R. Gomez, L. Lehner, B. Szilagyi, and J. Winicour, *Cauchy-characteristic matching*, arXiv:gr-qc/9801070.
[91] Michael J. Koop and Lee Samuel Finn, *Physical response of light-time gravitational wave detectors*, Phys. Rev. D **90**, 062002 (2014).
[92] Thibault Damour, *On some links between mathematical physics and physics in the context of general relativity*, *Physics on Manifolds* (Springer, Amsterdam, 1994), pp. 59–65.
[93] Nigel T. Bishop and Luciano Rezzolla, *Extraction of gravitational waves in numerical relativity*, Living Rev. Relativity **19**, 2 (2016).
[94] Franz E. Schunck and Eckehard W. Mielke, *General relativistic boson stars*, Classical Quantum Gravity **20**, R301 (2003).
[95] Richard Brito, Vitor Cardoso, Carlos A. R. Herdeiro, and Eugen Radu, *Proca stars: Gravitating Bose–Einstein condensates of massive spin 1 particles*, Phys. Lett. B **752**, 291 (2016).
[96] Carlos A. R. Herdeiro, Alexandre M. Pombo, and Eugen Radu, *Asymptotically flat scalar, Dirac and Proca stars: Discrete vs. continuous families of solutions*, Phys. Lett. B **773**, 654 (2017).
[97] C. Herdeiro, I. Perapechka, E. Radu, and Ya. Shnir, *Asymptotically flat spinning scalar, Dirac and Proca stars*, Phys. Lett. B **797**, 134845 (2019).
[98] Vitor Cardoso and Paolo Pani, *Testing the nature of dark compact objects: A status report*, Living Rev. Relativity **22**, 4 (2019).
[99] F. H. Vincent, Z. Meliani, P. Grandclement, E. Gourgoulhon, and O. Straub, *Imaging a boson star at the Galactic center*, Classical Quantum Gravity **33**, 105015 (2016).
[100] Carlos A. R. Herdeiro, Alexandre M. Pombo, Eugen Radu, Pedro V. P. Cunha, and Nicolas Sanchis-Gual, *The imitation game: Proca stars that can mimic the Schwarzschild shadow*, J. Cosmol. Astropart. Phys. 04 (2021) 051.
[101] Ahmed Almheiri, Donald Marolf, Joseph Polchinski, and James Sully, *Black holes: Complementarity or firewalls?*, J. High Energy Phys. 02 (2013) 062.
[102] R. Alves Batista *et al.*, *EuCAPT White Paper: Opportunities and challenges for theoretical astroparticle physics in the next decade*, arXiv:2110.10074.
[103] Lam Hui, Jeremiah P. Ostriker, Scott Tremaine, and Edward Witten, *Ultralight scalars as cosmological dark matter*, Phys. Rev. D **95**, 043541 (2017).
[104] R. D. Peccei and Helen R. Quinn, *CP Conservation in the Presence of Instantons*, Phys. Rev. Lett. **38**, 1440 (1977).
[105] Asimina Arvanitaki, Savas Dimopoulos, Sergei Dubovsky, Nemanja Kaloper, and John March-Russell, *String axiverse*, Phys. Rev. D **81**, 123530 (2010).
[106] Felipe F. Freitas, Carlos A. R. Herdeiro, António P. Morais, António Onofre, Roman Pasechnik, Eugen Radu, Nicolas Sanchis-Gual, and Rui Santos, *Ultralight bosons for strong gravity applications from simple standard model extensions*, J. Cosmol. Astropart. Phys. 12 (2021) 047.
[107] Steven L Liebling and Carlos Palenzuela, *Dynamical boson stars*, Living Rev. Relativity **20**, 5 (2017).
[108] Miguel Bezares, Carlos Palenzuela, and Carles Bona, *Final fate of compact boson star mergers*, Phys. Rev. D **95**, 124005 (2017).
[109] Carlos Palenzuela, Paolo Pani, Miguel Bezares, Vitor Cardoso, Luis Lehner, and Steven Liebling, *Gravitational wave signatures of highly compact boson star binaries*, Phys. Rev. D **96**, 104058 (2017).
[110] N. Sanchis-Gual, C. Herdeiro, E. Radu, J. C. Degollado, and J. A Font, *Numerical evolutions of spherical Proca stars*, Phys. Rev. D **95**, 104028 (2017).
[111] Edward Seidel and Wai-Mo Suen, *Formation of solitonic stars through gravitational cooling*, Phys. Rev. Lett. **72**, 2516 (1994).
[112] F. Di Giovanni, N. Sanchis-Gual, Carlos A. R. Herdeiro, and José A. Font, *Dynamical formation of Proca stars and quasistationary solitonic objects*, Phys. Rev. D **98**, 064044 (2018).
[113] N. Sanchis-Gual, F. Di Giovanni, M. Zilhão, C. Herdeiro, P. Cerdá-Durán, J. A. Font, and E. Radu, *Nonlinear dynamics of spinning bosonic stars: Formation and stability*, Phys. Rev. Lett. **123**, 221101 (2019).
[114] F. Di Giovanni, N. Sanchis-Gual, P. Cerdá-Durán, M. Zilhão, C. Herdeiro, J. A Font, and E. Radu, *Dynamical bar-mode instability in spinning bosonic stars*, Phys. Rev. D **102**, 124009 (2020).
[115] N. Sanchis-Gual, M. Zilhão, C. Herdeiro, F. Di Giovanni, J. A. Font, and E. Radu, *Synchronized gravitational atoms from mergers of bosonic stars*, Phys. Rev. D **102**, 101504(R) (2020).
[116] N. Sanchis-Gual, J. C. Bustillo, C. Herdeiro, E. Radu, J. A. Font, S. H. W. Leong, and A. Torres-Forne, *Impact of the wavelike nature of Proca stars on their gravitational-wave emission*, Phys. Rev. D **106**, 124011 (2022).
[117] Frank Loffler, Joshua Faber, Eloisa Bentivegna, Tanja Bode, Peter Diener, Roland Haas, Ian Hinder, Bruno C. Mundim, Christian D. Ott, Erik Schnetter, Gabrielle Allen, Manuela Campanelli, and Pablo Laguna, *The Einstein Toolkit: A community computational infrastructure for relativistic astrophysics*, Classical Quantum Gravity **29**, 115001 (2012).
[118] Miguel Zilhão and Frank Loffler, *An introduction to the Einstein Toolkit*, Int. J. Mod. Phys. A **28**, 1340014 (2013).
[119] Erik Schnetter, Scott H Hawley, and Ian Hawke, *Evolutions in 3D numerical relativity using fixed mesh refinement*, Classical Quantum Gravity **21**, 1465 (2004).
[120] Tom Goodale, Gabrielle Allen, Gerd Lanfermann, Joan Massó, Thomas Radke, Edward Seidel, and John Shalf, *The Cactus framework and toolkit: Design and applications*, in *Proceedings of the 5th International Conference*

on Vector and Parallel Processing (VECPAR'2002) (Springer, Berlin, 2003).

[121] Miguel Zilhão, Helvi Witek, and Vitor Cardoso, *Nonlinear interactions between black holes and Proca fields*, Classical Quantum Gravity **32**, 234003 (2015).

[122] Helvi Witek, Miguel Zilhao, Giuseppe Ficarra, and Matthew Elley, *Canuda: A public numerical relativity library to probe fundamental physics*, https://zenodo.org/records/3565475.

[123] C. Palenzuela, I. Olabarrieta, L. Lehner, and Steven L. Liebling, *Head-on collisions of boson stars*, Phys. Rev. D **75**, 064005 (2007).

[124] Curt Cutler and Eanna E. Flanagan, *Gravitational waves from merging compact binaries: How accurately can one extract the binary's parameters from the inspiral wave form?*, Phys. Rev. D **49**, 2658 (1994).

[125] J. Calderón Bustillo, P. Laguna, and D. Shoemaker, *Detectability of gravitational waves from binary black holes: Impact of precession and higher modes*, Phys. Rev. D **95**, 104038 (2017).

[126] Philip B. Graff, Alessandra Buonanno, and B. Sathyaprakash, *Missing link: Bayesian detection and measurement of intermediate-mass black-hole binaries*, Phys. Rev. D **92**, 022002 (2015).

[127] Juan Calderon Bustillo, Nicolas Sanchis-Gual, Samson H. W. Leong, Koustav Chandra, Alejandro Torres-Forne, Jose A. Font, Carlos Herdeiro, Eugen Radu, Isaac C. F. Wong, and T. G. F. Li, companion paper, *Searching for vector boson-star mergers within LIGO-Virgo intermediate-mass black-hole merger candidates*, Phys. Rev. D **108**, 123020 (2023).

[128] R. Abbott *et al.* (LIGO Scientific Collaboration, Virgo Collaboration, and KAGRA Collaboration), *Search for intermediate-mass black hole binaries in the third observing run of Advanced LIGO and Advanced Virgo*, Astron. Astrophys. **659**, A84 (2022).

[129] Within our simulation set [127], we found that this was typically the lowest value leading to no secular drifts. As we note, however, in some cases this choice removes "true signal power" from the detector band. In particular, for the total masses chosen for our GW190521-like and S200114f-like injections, our cutoff frequency $M\omega_0$ translates to 32.3 and 37.2 Hz, respectively.

[130] Joshua S. Speagle, *DYNESTY: A dynamic nested sampling package for estimating Bayesian posteriors and evidences*, Mon. Not. R. Astron. Soc. **493**, 3132 (2020).

[131] R. Abbott *et al.* (LIGO Scientific Collaboration and Virgo Collaboration), *GW190521: A binary black hole merger with a total mass of* $150M_\odot$, Phys. Rev. Lett. **125**, 101102 (2020).

[132] LIGO Scientific Collaboration, *LIGO algorithm library—LALSuite*, https://lscsoft.docs.ligo.org/lalsuite/lalsuite/index.html.

[133] John Veitch, Walter Del Pozzo, Alex Lyttle, Michael Williams, Colm Talbot, Matt Pitkin, Gregory Ashton, Cody, Moritz Hübner, Alex Nitz, Duncan Macleod, Gregorio Carullo, Guy Davies, and Tony, johnveitch/cpnest: v0.11.3, https://github.com/johnveitch/cpnest.

[134] Rory J. E. Smith, Gregory Ashton, Avi Vajpeyi, and Colm Talbot, *Massively parallel Bayesian inference for transient gravitational-wave astronomy*, Mon. Not. R. Astron. Soc. **498**, 4492 (2020).

[135] Here, we make the crude assumption that, for suitable combinations of the binary parameters, one shall obtain similar merger-ringdown signals as those obtained for our head-on mergers.

[136] S. Klimenko *et al.*, *Method for detection and reconstruction of gravitational wave transients with networks of advanced detectors*, Phys. Rev. D **93**, 042004 (2016).

[137] J. D. Merritt, Ben Farr, Rachel Hur, Bruce Edelman, and Zoheyr Doctor, *Transient glitch mitigation in Advanced LIGO data*, Phys. Rev. D **104**, 102004 (2021).

[138] Mark Hannam, Charlie Hoy, Jonathan E. Thompson, Stephen Fairhurst, Vivien Raymond, Marta Colleoni, Derek Davis, Héctor Estellés, Carl-Johan Haster, Adrian Helmling-Cornell *et al.*, *General-relativistic precession in a black-hole binary*, Nature (London) **610**, 652 (2022).

[139] Frank Ohme, *Bridging the gap between post-Newtonian theory and numerical relativity in gravitational wave data analysis*, Ph.D. Thesis, Universitat Potsdam, 2012.

[140] For two similar examples, concerning environmental effects on black-hole mergers and thermal effects in neutron star mergers, please see [141,142].

[141] Samson H. W. Leong, Juan Calderón Bustillo, Miguel Gracia-Linares and Pablo Laguna, *Impact of ringdown higher-order modes on black-hole mergers in dense environments: The scalar field case, detectability and parameter biases*, arXiv:2308.03250.

[142] Verónica Villa-Ortega, Ana Lorenzo-Medina, Juan Calderón Bustillo, Milton Ruiz, Davide Guerra, Pablo Cerdá-Duran, and José A. Font, *Self-consistent treatment of thermal effects in neutron-star post-mergers: Observational implications for third-generation gravitational-wave detectors*, arXiv:2310.20378.

[143] Samantha A. Usman *et al.*, *The PyCBC search for gravitational waves from compact binary coalescence*, Classical Quantum Gravity **33**, 215004 (2016).

[144] C. Messick, K. Blackburn, P. Brady, P. Brockill, K. Cannon, R. Cariou, S. Caudill, S. J. Chamberlin, J. D. E. Creighton, R. Everett *et al.*, *Analysis framework for the prompt discovery of compact binary mergers in gravitational-wave data*, Phys. Rev. D **95**, 042001 (2017).

[145] Ian Harry, Juan Calderón Bustillo, and Alex Nitz, *Searching for the full symphony of black hole binary mergers*, Phys. Rev. D **97**, 023004 (2018).

[146] F. Aubin, F. Brighenti, R. Chierici, D. Estevez, G. Greco, G. M. Guidi, V. Juste, F. Marion, B. Mours, E. Nitoglia, O. Sauter, and V. Sordini, *The MBTA pipeline for detecting compact binary coalescences in the third LIGO–Virgo observing run*, Classical Quantum Gravity **38**, 095004 (2021).

[147] Qi Chu, Manoj Kovalam, Linqing Wen, Teresa Slaven-Blair, Joel Bosveld, Yanbei Chen, Patrick Clearwater, Alex Codoreanu, Zhihui Du, Xiangyu Guo, Xiaoyang Guo, Kyungmin Kim, Tjonnie G. F. Li, Victor Oloworaran, Fiona Panther, Jade Powell, Anand S. Sengupta, Karl Wette, and Xingjiang Zhu, *SPIIR online coherent pipeline to search for gravitational waves from*

compact binary coalescences, Phys. Rev. D **105**, 024023 (2022).

[148] Koustav Chandra, Juan Calderón Bustillo, Archana Pai, and I. W. Harry, *First gravitational-wave search for intermediate-mass black hole mergers with higher-order harmonics*, Phys. Rev. D **106**, 123003 (2022).

[149] https://git.ligo.org/samson.leong/bilby-extra.

[150] Rich Abbott *et al.*, *Open data from the first and second observing runs of Advanced LIGO and Advanced Virgo*, SoftwareX **13**, 100658 (2021).

[151] R. Abbott *et al.* (LIGO Scientific Collaboration, Virgo Collaboration, and KAGRA Collaboration), *Open data from the third observing run of LIGO, Virgo, KAGRA and GEO*, arXiv:2302.03676.